Viscous Fingering in Radially-Tapered Fluidic Cells

by

Grégoire Bongrand

A thesis submitted in partial fulfillment of the requirements for the degree of

Master of Science

Department of Mechanical Engineering

University of Alberta

Abstract

This thesis work concerns the viscous fingering instability occurring during immiscible fluid-fluid displacement experiments using a novel radially-tapered fluidic cell. We use modified Hele-Shaw cells where a negative depth gradient is introduced by tapering the upper plate, so that the gap thickness linearly decreases in the flow direction. We experimentally show that when a less viscous fluid displaces a more viscous one in a converging cell, the classic Saffman-Taylor instabilities can be suppressed and surprisingly the possibility of achieving a full sweep.

Inspired by these observations, we study the feasibility of controlling such instabilities in non-uniform narrow passages with Newtonian fluids. In particular, we investigate the impact of gap gradient, α, on the stability, for different flow configurations. The injection flow rate, Q, has revealed to be a critical parameter manipulating the viscous fingering instability. For a fixed cell gradient (α), our experimental results show that a full sweep is achieved at low Q, whereas a partial displacement with fingering is obtained when Q overcomes a threshold. By using various cells of different α, we observe the variation of the critical threshold between stable and unstable displacements in terms of flow rate, Q, and the capillary number, Ca, characterizing the effects of viscous forces to surface tension. The comparison of our experimental results of critical Ca^* with the theoretical predictions by a recent linear stability analysis showed good agreement.

Numerous applications of the viscous fingering problem take place in rock formations, such as groundwater hydrology, soil remedy, and enhanced oil recovery. In such porous formations, there is a high chance of finding solid grains, mineral or debris in the fluid flows.

Hence, we extended our study on the viscous fingering instability in inhomogeneous passages by considering the displacement of a suspension. The interplay between the destabilizing effect of the particles and the stabilizing effect of the depth gradient is investigated for different particle concentrations, c_p. For a fixed α and c_p, surprisingly, it is still possible to achieve stable displacements when the injection pressure of gas, p, is smaller than a critical value. Finally, by systematically varying the particle concentration and/or the depth gradient, we characterize the variation of that critical threshold, in terms of critical gas pressure and interface velocity, delineating the full and partial sweep. By considering the influence of the micro-particles and the particle concentration, the establishment of a more complete and multi-dimensional viscous fingering stability diagram is revealed for the first time.

Preface

The whole experimental work presented in this thesis was performed by Grégoire Bongrand under the supervision of Dr. Peichun Amy Tsai.

Chapter 2 of the thesis is taken from the journal paper by Grégoire Bongrand and Peichun Amy Tsai, "Manipulation of viscous fingering in a radially tapered cell geometry." Physical Review E, Rapid Communications 97(6), 061101(R), 2018.

Chapter 3 forms a base of a manuscript in preparation by Grégoire Bongrand and Peichun Amy Tsai, "Effects of suspensions on the viscous fingering instability in a radially-tapered geometry", in preparation, 2018.

Acknowledgements

Firstly, I would like to express my sincere gratitude to my supervisor Dr. Peichun Amy Tsai for her research ideas, continuous support, constant discussion, training, education, and patience, which has helped me constantly progressing throughout the research project but also preparing for my future career.

I would also like to thank Bernie Faulkner whom I had the chance to work with, for his expertise, guidance, and support for the realization of the second experimental setup.

Thanks go to all the students who have been part of the group for the last two years and who made my Master study more enjoyable. A special thank to Adrien Bussonnière, Tsai-Hsing Ho, and Masoud Bozorg Bigdeli for their interesting discussions and suggestions on the experiments and analysis.

Finally, I would like to thank all my friends for their support and, I am particularly grateful to my parents and brother for all the love and support they give me throughout my whole education and life.

Contents

List of Figures

List of Tables

Chapter 1

Introduction

1.1 Porous Media Flow

The flow of fluids through porous media has attracted much interest due to various important applications such as groundwater hydrology, petroleum engineering, and industrial purification, etc. [1]. The fundamentals of the theory for porous media flow are complex because the flow takes place inside the pores, at a microscopic scale, and the extension of the fluid domain to the full porous medium by establishment of some length and time scales has been revealed to be difficult [2]. The complexity of the theory combined to the growing industry demand have led to the derivation of several empirical observations and simplified theoretical models that helped with the understanding, which will be discussed briefly below.

A porous medium is a material or domain containing voids that can be filled by a fluid (liquid or gas), such as rocks or soils. It is generally characterized by its porosity, φ, a measure of the pore space defined by the ratio of the volume of voids to the total volume. This definition is also known as the 'total' porosity, while the 'effective' porosity is restricted and does not include the space occupied by rock debris and an eventual thin layer of water surrounding the mineral surfaces in the volume of voids [1, 3]. In addition to the porosity, the size of the pores and the distribution of the pore size are also relevant

parameters to characterize a porous medium. Another important parameter characterizing a porous medium is the permeability. The absolute permeability—an intrinsic property of the medium, independent of the fluid properties—describes the capacity of one single-phase fluid to flow through it, when subjected to a pressure difference. In this thesis, the fluids considered are incompressible, Newtonian and immiscible unless precised. For a single-phase fluid flowing through a porous medium at a constant elevation, the absolute permeability, k, is linked to the discharge of fluid, Q, (volume of fluid flow per unit time) and the pressure difference, Δp, according to the Darcy's law expressed as [2]:

$$Q = -\frac{kA}{\mu L}\,\Delta p \tag{1.1}$$

where μ is the fluid viscosity, L the length over which the pressure drop applies, and A the cross-sectional area of the flow. Hence, by setting a flow of a known-viscosity fluid at a controlled flow rate, Q, and pressure difference, Δp, inside the porous structure, its absolute permeability can be derived from Eq. 1.1 [3]. In addition, there were several attempts at finding empirical relations to measure the absolute permeability of the medium, based on geometrical properties such as the porosity. However, they were not very successful as the multiplicative constants found were never unique [1]. One common mathematical technique to estimate the absolute permeability of a porous medium considers using simple assumptions of modelling, such as modelling the porous medium by a pack of beads or a network of capillaries [1]. We recall these observations are valid for single-phase flow only.

Moreover, on many occasions, multiphase porous media flows are of particular interest. It was first thought that the absolute permeability of the medium in Eq. 1.1 could be valid for any fluid and mixture of fluids, but some experiments revealed that the presence of the second phase decreases significantly the permeability of the first phase [1]. Hence, Muskat [3] suggested that Darcy's law can be extended to multiple phase flow and introduced the concept of relative permeability, k_i, of a phase indexed i. Therefore, for a steady, Stokes flow of multiple phases through a horizontal porous medium (i.e., gravity is neglected), the phase velocity, $\vec{V}_i$, is expressed as:

$$\vec{V}_i = -k\frac{k_i}{\mu_i}\,\vec{\nabla} P \tag{1.2}$$

where μ_i is the phase viscosity, and k_i is the relative permeability, expressed as a fraction of the absolute permeability, k, and is generally a tensor quantity. One can define also the mobility of the phase i, M_i, in the fluid domain, taking into account both the fluid and medium properties, as the ratio $M_i = kk_i/\mu_i$. This mobility parameter is most commonly used to characterize porous media flows.

When a fluid phase displaces another immiscible one in a porous medium, the fluid-fluid interface advances at a speed V described by Eq. 1.2. The motion of the interface is driven by the forces exerted on it, such as the interfacial and surface tensions as well as the hydrodynamic forces [4]. The influence of these forces can be characterized by the dimensionless Capillary (ratio of the viscous forces to the surface tension), Weber (ratio of the inertia effects to the surface tension), and Bond (ratio of the gravitational effects to the surface tension) numbers, defined as [5]:

$$Ca = \frac{\mu V}{\gamma},\ We = \frac{\rho V^2 l}{\gamma},\ Bo = \frac{\Delta\rho g l^2}{\gamma}, \tag{1.3}$$

respectively, where ρ is the density of the appropriate fluid, γ is the interfacial tension, and l is the characteristic length. The importance of one force compared to another and the approximations to neglect some contributions in specific cases are discussed in [5]. For horizontal flows in porous media applications, l is usually small enough so that the Weber and Bond numbers can be neglected, and the capillary number then becomes the most predominant factor [4]. However, this assumption is not true for some applications in vertical porous media such as packed towers [6], where the contributions of the characteristic length and gravity cannot be neglected.

1.2 Applications

Porous materials are widely present around us and play a crucial role in various aspects of our daily lives. Sand, sandstone, soil, fissured rock, wood, sponge, plant leaves, bones, and lungs, are just a few examples of porous materials that can be encountered in nature [7]. Artificial porous materials such as wicks, textile, ceramic, foam rubber, industrial filters,

catalysts, etc. are also prevalent and commonly used in the industry [8]. Natural and artificial porous structures are found in a great variety of fields such as energy management, vibration suppression, heat insulation, sound absorption, and fluid filtration [8].

Multiphase flows in porous media are common in both nature and industry and find a wide range of applications. The most important areas of technology where porous media flows play an important role are hydrology, which consists of the motion of water in the earth and sand structures, and petroleum engineering, which studies oil and natural gas production, exploration, well drilling, etc. [2]. Furthermore, flows through porous materials are encountered in many other sciences such as in chemical engineering with chromatography, filtering processes etc., in biomedical engineering with the flow of blood, biological membranes, etc., or also sintering of granular materials such as the manufacture of ceramic, paper, leather, textile, rubber, etc. [2].

Due to the abundance of applications, the mechanisms and interactions between two fluid flowing through (reconstructed) porous structures have been studied intensively. The interest in such fluid-fluid displacements also gained even more attention since the development of some instabilities at the interface has been observed in some cases. In some specific situations, the formation of such patterns can be beneficial, and it helps us understand the mechanisms that lead to the occurrence of similar patterns found in nature [9, 10]. However, in many other applications, the instabilities disrupt the conduct of the process and reduce the efficiency. A few examples of applications where interfacial instabilities have been observed in fluid-fluid displacements are sugar refining operations [11], coating flows and printing devices [12, 13, 14, 15, 16, 17], CO_2 geological sequestration [18, 19, 20, 21, 22], and enhanced oil recovery [23, 24, 25]. Coating flows and enhanced oil recovery are two examples we will discuss where instabilities are not desired.

A coating flow is a fluid flow where a thin, uniform layer is deposited on a surface called a substrate, often used to protect or decorate the surface [16]. For instance, the application of paint by a roller [13] or a brush and printing devices [26] are classic examples of coating flows. Once applied for an industrial purpose, some constraints of productivity

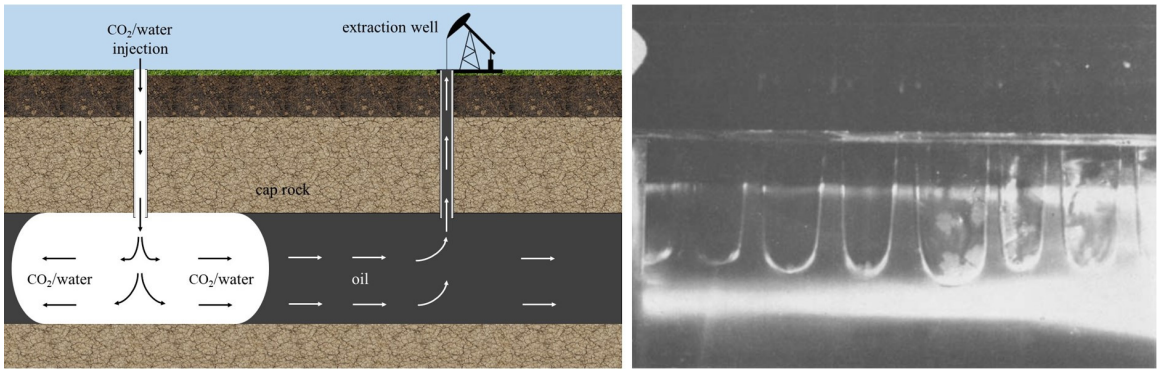

Figure 1.1: Fluid-fluid displacement applications. The left panel is a schematic side view of enhanced oil recovery process. The right panel, extracted from [14], shows the development of air fingers when confined oil flows between a roller and a diverging plate

may rise such as using a high velocity or a multiple layer deposition. However, under such restrictions, the deposited layer may not be uniform, and some interfacial instabilities in the form of waves or streaks may appear [12, 13, 14] (see Fig. 1.1). Opposite to the purpose of a coating of having a uniform fluid layer, the formation of these patterns is therefore not desired and disrupt the operation.

Enhanced oil recovery (EOR) consists in injecting gas or chemicals into an underground reservoir so that the surrounding oil can be pushed away from the injection source and extracted from another well for recovery [23, 24] (see Fig. 1.1). This operation can also be associated with CO_2 geological sequestration where the CO_2 is stored underground via trapping under a cap rock, sinking plumes, and formation of carbonate minerals [22]. In enhanced oil recovery applications, the development of instabilities at the interface would result in significant amounts of oil left behind, which is dramatic for the purpose of such a process. What's more, during oil extraction, it was observed that water or CO_2 may break through and reach the extracting well after only a small amount of the predicted oil volume has been recovered [4]. For instance, in some laboratory experiments [27], only 13% of the initial oil volume was extracted for a specific configuration, while it should have been over 40% according to [28]. Consequently, excessive quantities of water and CO_2 must be injected to expel greater oil proportions, and sometimes several fluid injections are performed. Hence, this surplus of injected fluid directly impacts both the economic and

environmental aspects of the process and makes it less efficient [24]. Besides the extraction efficiency, the mechanisms describing the pattern formation and growth were not well understood. Therefore, the subject of unfavorable fluid-fluid displacement in porous media has been extensively studied since the 1950s.

1.3 Viscous fingering in Hele–Shaw cells

When a less mobile fluid is displaced by another more mobile, immiscible one in a porous medium, instabilities may arise at the interface and propagate in the shape of fingers: this phenomenon is called viscous fingering [11]. Those perturbations will grow and evolve throughout the process, leading to complex, non-linear pattern formations that alter the flow considerably (see Fig. 1.2). The magnitude and morphology of these instabilities are greatly dependent on various parameters which we discuss in the next sections.

Since most porous materials are opaque, the direct visualization of the flow is obstructed and qualitative observations on the pattern formation cannot be easily realized. Therefore, viscous fingering has been mostly observed and studied in a convenient, transparent analogy: a Hele–Shaw cell. A Hele–Shaw cell consists of two parallel plates separated by a small gap h_0 that recreates a quasi two-dimensional (2D), homogeneous porous medium [29]. The fluid mobility inside a Hele–Shaw cell is defined by the gap thickness and the fluid viscosity, giving rise to an equivalent permeability k that is constant and defined as: $k = h_0^2/12$. This latter expression is derived from the derivation of the average velocity as a function of the pressure gradient for a plane Poiseuille flow . The porosity of a Hele–Shaw cell is one since only void is present. Some essential features of a porous medium, such as the heterogeneous pore structure and distribution, are not captured for a homogeneous Hele–Shaw flow. Nevertheless, this simple geometry turns out to be convenient to understand quasi-2D pattern morphology and reflect on more complex problems.

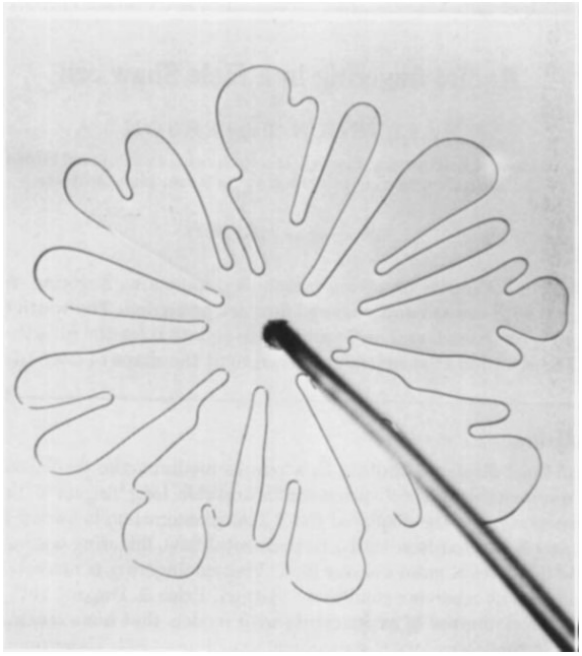

Figure 1.2: Viscous fingering pattern when air displaces glycerine in a radial Hele–Shaw cell [30]. (Figure is extracted from [30]).

1.3.1 With Newtonian fluids

The first viscous fingering studies were reported using Newtonian fluids, due to their simple rheological properties. Saffman & Taylor conducted the first viscous fingering experiment in Hele–Shaw cells [31] and observed systematically the emergence of instabilities. Since then, this so-called Saffman-Taylor instabilities have been extensively investigated in Hele–Shaw cells. In the following discussions, the fluid-fluid interaction is immiscible unless stated.

In a rectangular Hele–Shaw cell, after an initial wavy front, one dominating, displacing finger forms and evolves nearly steadily in the centre of the cell throughout the process [4, 31, 32, 33, 34, 35, 36]. The width of the finger decreases with increasing velocity and, at high velocities, reaches a plateau of a constant value which is about half the channel width [31, 32, 34]. With an increasing gap thickness, the finger grows wider, but the plateau value remains the same [34]. It has been observed that the relative width of the finger (ratio of the finger to channel widths) follows a unique curve when scaled with the parameter $1/B = Ca\,\delta^2$ [34, 35], with δ the ratio of the channel width to gap thickness. When the

displaced fluid perfectly wets the cell, a thin liquid film is left behind, and its thickness increases with an increasing Ca [35]. Saffman & Taylor theoretically predicted that the finger should be unstable at finite and infinite Ca but observed only stable fingers in their experiments [31]. While some works later revealed the occurrence of tip-splitting at higher values of Ca, experimentally [35, 37] and numerically [36].

Rectangular Hele–Shaw cells have long been an excellent platform to study homogeneous viscous fingering, while radial injections are also relevant to study the EOR process. The stability studies of radial Hele–Shaw flows have been considered first theoretically by Bataille [38] and experimentally by Paterson [30]. When the displacing less-viscous fluid is injected at a constant rate, an early circular interface forms and then becomes wavy before several fingers eventually appear and develop symmetrically. Paterson theoretically characterized the destabilization of the circular interface when its circumference exceeds a critical wavelength, which depends on its radius, the injection flow rate, the surface tension, and the outer fluid mobility [30]. By considering a quasi-infinite, symmetric radially propagating finger, a linear stability analysis [30] showed that the fingering morphology obtained in the experiments is well predicted by the theory. The formation of similar symmetric finger shapes have also been well described by numerical calculations [39]. However, experimental observations revealed that it is also possible to obtain asymmetric fingers. At later times, experimental observations and theoretical predictions showed that the finger grows wider throughout the displacement until it eventually splits at the tip, resulting in two "sub-fingers" [30, 39, 40]. By combining the formation of symmetric and asymmetric fingers with repetitions of tip-splitting mechanism, a complex, branch-like structure can emerge during the radial Saffman-Taylor problem. The fingering morphology varies depending on the flow rate and goes from compact to narrower fingers with side-branches as the flow rate increases [40].

Contrary to viscous fingering in rectangular channels [41], the number of fingers increases as the interface radially advances [30, 39, 40]. Chen [40] investigated the effect of plate roughness and showed that dendritic or needle-like fingers can develop at sufficiently

high values of flow rate and roughness. Chen characterized the finger pattern "age" based on the tip-splitting generation, i.e., the number of tip-splitting that occurred for one branch [42]. Two identical experiments may result in different patterns but, at the same generation of splitting or same dimensionless time, the fingers have similar morphologies [42]. Surprisingly, the fractal behaviour of the patterns is revealed only after a few generations of splitting, and the fractal dimension varies from 1.82 to 1.9 in [42] and 1.69 to 1.92 in [43]. As the Saffman-Taylor instability is dominated mostly by the viscosity difference of the pair of the fluids, an experimental study focused on the impact of the viscosity ratio on the pattern morphology [44]. In radial Hele−Shaw cells, the interface always gets unstable as long as the viscosity ratio $\mu_{out}/\mu_{in} > 1$ (i.e., the viscosity ratio between the outer and inner fluids), but the inner stable region increases with a decreasing viscosity ratio. The length of the fingers was revealed to depend on the viscosity ratio and radius of the inner circular region [44].

1.3.2 With complex fluids

The use of Newtonian fluids was essential to understand the mechanism of pattern formation in viscous fingering problems. However, the increasing use of complex fluids, such as polymers or surfactants, in industrial applications has led to a recent increasing interest in viscous fingering problems with complex fluids. Additionally, suspensions and granular mixtures have also been investigated because of the frequent presence of solid grains and debris when performing fluid-fluid displacements in porous geological structures and rock fractures [45].

Generally, complex fluids are made of two or more distinct phases: liquid-gas such as foams, liquid-liquid such as emulsions, solid-liquid such as suspensions or polymers and solid-gas such as granular mixtures [46]. The coexistence of multiple phases can lead to complex and nonlinear mechanical responses to applied stress or strain, and these fluids are denoted as non-Newtonian and/or elastic fluids. A non-Newtonian fluid is a liquid or a gas whose viscosity does not follow the linear Newtonian viscosity law. The viscosity

of Newtonian fluids is constant and given as the slope of the curve of the shear stress along the shear strain. The viscosity of non-Newtonian fluids can be constant if the fluids require a finite yield stress to start to flow, in which case they are called Bingham fluids [46]. Otherwise, the viscosity of non-Newtonian fluids which are not Bingham fluids is not constant and can either increase (shear-thickening fluids) or decrease (shear-thinning fluids) with an increasing shear strain [46]. Some complex fluids are elastic too and they deform when a stress is applied before coming back to their original state upon release of the stress. When the fluids exhibit both elastic and viscous effects, they are characterized as visco-elastic fluids [46]. Here, we present some complex fluids that have been often studied in the viscous fingering problems to show how the viscosity, surface tension, and elasticity can alter the interface stability.

A. Surfactants

One type of complex fluids used in viscous fingering problems is surfactant solutions, which lead to displacements where the interfacial tension is significantly reduced (i.e., increase in Ca). For the Saffman-Taylor problem in linear cells, the finger width decreases with increasing surfactant concentration [47, 48]. Similarly to the classic problem, the relative finger width with surfactants decreases with an increasing velocity before reaching a plateau of higher value than the classical limit 1/2. However, at low surfactant concentration, the finger width decreases with an increasing velocity, until reaching a minimum, before slightly increasing and reaching a plateau of value even bigger [47]. The addition of surfactant in the inverse Saffman-Taylor problem, when an aqueous surfactant solution displaces air in a pre-wetted rectangular Hele–Shaw cell, has also revealed to destabilize the interface when its velocity overcomes a critical velocity [49]. This velocity threshold slowly decreases with an increasing surfactant concentration and increases with an increasing gap thickness [49].

B. Polymers

Other studies with complex fluids that attracted much attention are the viscously-unfavorable experiments using polymers, which sometimes offer the possibility of presenting viscous and elastic effects at once. It has been shown that, for polymers exhibiting only elastic effects such as polyethylene oxide (PEO), the finger width in rectangular cells decreases with increasing interfacial velocity before reaching a plateau at a higher value than the classical limit 1/2 [47, 48]. For higher polymer concentrations, the width surprisingly reaches a minimum before increasing and reaching a plateau of even higher value. For non-elastic, shear-thinning polymers, such as Xanthan, the finger width decreases with an increasing polymer concentration, and fingers are narrower than those for Newtonian case [48, 50]. The relative width of the finger follows the universal curve over $1/B$ if the viscosity μ is replaced by the shear-rate dependent of $\mu(\dot{\gamma})$ for weak shear-thinning effects. For stronger shear-thinning effects, the relative width of the finger follows the unique curve over $1/B(\mu(\dot{\gamma}))$ only at small values of $1/B$ [48, 50]. For strong shear-thinning, an expression of the velocity derived from the power-law model is shown to describe better the flow behaviour than the effective Darcy's law, where μ is replaced by $\mu(\dot{\gamma})$ [50].

Experiments with yield stress fluids which present shear-thinning behaviour revealed that at low velocities the structure is ramified (with more than one finger) and has a width that is independent of the velocity or the channel width but increases with an increasing gap thickness [51, 52, 53]. On the other hand, at higher velocities, only one single, stable finger is present and gets narrower with an increasing velocity before reaching a plateau value smaller than half the channel width. The relative finger width is found to follow a unique curve not proportional to $Ca\,\delta^2$ but to $Ca\,\delta$ according to [51], and to $Ca\,\delta^{n+1}$ for [53]. The transition between yield stress and viscous regimes is found to be at fixed parameter of $Ca\,\delta^{n+1}/Bn$ [53], with Bn the Bingham number being the ratio of the yield stress over viscous stress. At even higher velocities and lower yield stresses, there is a formation of side-branches along the finger but no tip-splitting occurrence [52, 53]. Similar qualitative observations were also seen in radial injections [52].

Some studies using shear-thinning, associating polymers revealed the formation of side-branches with angles around 90° when the injection rate is bigger than a critical threshold (but not valid for homopolymers) [54, 55]. The transition between viscous and fracture-like regimes is characterized by a constant Deborah number, De, and a dramatic decrease in the fractal dimension [54]. For polymers with low molecular weights, the pattern goes from a viscous finger shape to a crack pattern, and an abrupt increase of the velocity is observed. For high molecular weights, the transition leads to a meandering structure with some slight side-branches, and is characterized by a gradual increase of the velocity [55].

C. Colloids

Several investigations have dealt with viscous fingering using suspensions or colloidal solutions. Sometimes, solutions of suspensions associated with some polymers can be shear-thinning, and similar results as for single-phase shear-thinning polymers were found [56].

Most of the time, suspensions in a liquid mixture are shear-thickening, and new characteristics of viscous fingering are observed. With an increasing particle concentration or flow rate, the pattern morphology in a radial injection goes from viscous fingering to visco-elastic fracturing manifested by cracks, as observed in [57, 58], or to side-branching [59]. It was shown that the denser is the suspension, the smaller is the critical flow rate separating the two regimes of viscous fingering and visco-elastic fracturing. In rectangular channels, a transition to tip-splitting and side-branching was observed during the process [56, 60]. The latter study showed that the onset of instabilities decreases with an increase in the particle concentration, in the injection pressure, or with a decrease in the gap thickness. The onset of instabilities is quantitatively characterized by a critical shear rate, $2V/h_0$, which is independent of the injection pressure or the gap thickness but decreases with an increasing particle concentration [56, 60]. The finger width increases with a denser solution, whereas an increase in the injection pressure narrows the fingers and enhances the tip-splitting occurrence. The effective Darcy's law, using the shear-rate dependent viscosity, $\mu(\dot{\gamma})$, was shown to be valid for weak shear-thickening effects. However, for stronger

shear-thickening effects, the correlation between the experimental velocity and the effective Darcy's law velocity is valid only for small values of the experimental velocity.

Introducing particles in the more-viscous fluid for the inverse Saffman-Taylor problem can destabilize a normally-stable interface as shown in [61, 62, 63, 64]. It has been observed that the onset of instabilities depends strongly on the particle concentration, c_p, and aspect ratio gap thickness (h) over particle size (d), $\frac{h}{d}$. In [63, 64], a stability diagram depending on c_p and $\frac{h}{d}$ was established experimentally, the researchers showed that a necessary condition to obtain fingering is that the mean particle velocity is greater than the bulk mean velocity far upstream of the interface. However, the magnitude of fingering depends mostly on the total amount of accumulated particles at the interface [63]. An increase in the particle concentration or aspect ratio leads to a decreasing onset of instabilities [62, 63, 64]. The inverse Saffman-Taylor problem where particles are captured by an advancing front [62] revealed that the symmetry of the pattern and the sweep efficiency depend greatly on Ca. When Ca is bigger than a critical threshold, the interface extends symmetrically and compact fingers are propagating together, whereas for values of Ca smaller than the threshold, a few fingers form in some preferential directions and the amount of displaced fluid extracted is much smaller.

In short, viscous fingering problems with complex fluids have been widely investigated and revealed eventual non-linear patterns, such as cracks or side-branches. Similar observations as for the classical Saffman-Taylor problem with simple fluids were derived, with the finger width that decreases with an increasing velocity. While the presence of surfactants at the interface seems to increase the relative width of the finger compared to pure, Newtonian systems, the rheological behaviours of polymer or colloidal solutions must be investigated first to predict the pattern morphology. Generally, for the displacement of suspensions, the fingers are wider than pure fluids, and the onset of instabilities is decreased with an increasing particle concentration and increasing injection pressure. For the displacement of polymer solutions, the results are highly dependent on the fact the polymer is purely viscous, purely elastic, or visco-elastic. The fingers emerging when displacing purely elastic polymer

solutions are wider than those of the classical Newtonian case, whereas narrower fingers are obtained when pushing purely viscous polymers presenting shear-thinning effects. Finally, for visco-elastic polymers presenting for example both yield stress and shear-thinning effects, a distinction of the different regimes is necessary to predict the pattern morphology.

1.4 Control of viscous fingering

Since the pattern formation of viscous fingering can be either beneficial or detrimental depending on the particular goals of the applications, the feasibility of controlling the patterns for a well-known configuration is extremely helpful. Nevertheless, no study had shown good solutions to suppress viscous fingering and make the interface (almost) stable. Recently, the control of viscous fingering has been examined even more thoroughly using modified flow cells, with different fluid properties, or using new techniques of injection.

For instance, for a pair of miscible fluids, the interfacial tension between the two fluids almost vanishes. For viscous fingering problems with miscible fluids, the length of the fingers become zero when the viscosity ratio decreases, and a stable interface can be obtained [65]. The effect of surface tension on the immiscible finger morphology has been investigated by perturbation theory approach where the surface tension is assumed to be depending on the interface curvature [66]. Exploring theoretically the viscous fingering problem assuming the surface tension increases with an increasing curvature (i.e., as the interface grows) has been shown to suppress the classic viscous fingers [66]. The researchers also revealed the possibility of destabilizing a normally-stable interface in the inverse Saffman-Taylor problem (more-viscous fluid displacing less-viscous one) by adopting the same assumption [66].

Another property that alters the pattern formation is the wettability of the porous medium. Some experimental work has been performed in Hele−Shaw cells where glass beads or pattern networks were introduced to control better the wettability, with contact angles varying from 5° to 150° [67, 68]. For a fixed Ca, as the contact angle of the displaced fluid increases (i.e., the invading fluid becomes more wetting), the pattern becomes more compact, and the fractal dimension increases.

1.4.1 Using a time-dependent injection process

Most of Hele–Shaw experiments mentioned previously have been performed with a constant flow rate of injection. A recent strategy presented to control the pattern evolution is adopting a varying injection rate during the process (see Fig. 1.3). Derived from a linear stability analysis [38, 69], varying the pumping flow rate over the time as $1/R \sim t^{-1/3}$, with R the interfacial radius, results in an unchanged pattern shape (i.e., number of fingers constant) throughout the process. Controlling the final shape of the interface adopting this time-dependent strategy on the flow rate was confirmed numerically and experimentally [70, 71, 72]. In addition, a theory based on harmonic moments of Laplacian growth studied the possibility of controlling the number of fingers during the radial spreading and showed a quite good agreement with experiments [71]. Instead of varying the injection rate, varying the cell gap thickness correspondingly with time with a constant flow rate resulted in a theoretically similar control for both immiscible [73] and miscible cases [72]. Similarly, an experimental study has been carried out for the case of a lifting plate with a gap thickness, $h(t)$, evolving as $t^{1/7}$ to show the possibility of hindering viscous fingering [74]. It has been showed that the number of fingers of the interface could be controlled by a theoretical, dimensionless parameter, $J = \frac{6\mu Q R(t)}{\pi\gamma h(t)^3}$, with Q the injection rate, γ the interfacial tension, and $R(t)$ the radius of the interface. When $h(t) \sim t^{1/7}$, the parameter J becomes time-independent and the validity of the model was verified via experiments [74]. However, even though this strategy can enhance the sweep efficiency, viscous fingering was still present in both experiments [74] and numerical simulations [72, 73], and some oil is left behind.

Finally, the possibility of suppressing viscous fingering was revealed by some theoretical studies, using a simple piecewise-constant pumping flow rate [77], and an injection rate that varies linearly with time [76]. The numerical simulations adopting a two-stage piecewise-constant injection flow rate show almost full sweep of the displaced fluid where viscous fingering is observed for a flow rate equivalent on average [77]. Remarkably, the suppression of viscous fingering using a linearly time-dependent, optimal flow rate, which is independent of the fluid properties or other factor such as plate lifting, is shown using linear stability

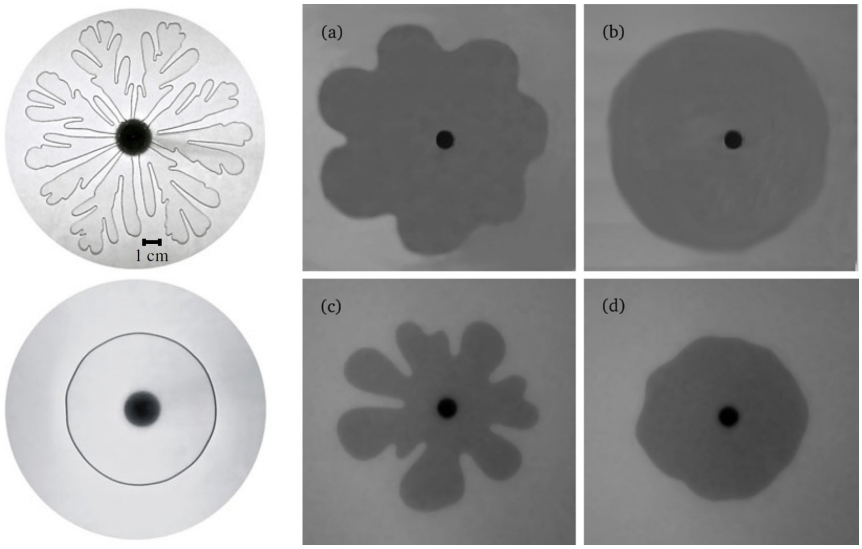

Figure 1.3: Suppression of viscous fingering manifested by stable displacements via different techniques. The left panel shows the control of the classic Saffman-Taylor instabilities when air displaces oil under an elastic membrane [75]. The right panel reveals the minimization of fingering by adopting a time-dependent flow rate of injection when water displaces oil in a Hele–Shaw cell [76]. (Figures are extracted from [75] (left), and [76] (right), respectively).

analysis predictions and experiments [76].

1.4.2 Changing the cell geometry

When we choose a pair of "simple" (as opposed to complex) fluids and a straightforward, constant injection process, one means of modifying the flow and eventually hinder the Saffman-Taylor instabilities relies on the fluidic cell geometry (see Fig. 1.3). Adopting a varying cell geometry would result in a non-constant permeability, as the permeability is directly proportional to the gap thickness, h, as $k = h^2/12$ as mentioned in §1.3.

A. Using an elastic membrane

Replacing one of the plates of the cell by an elastic sheet has been proven to delay, and even sometimes inhibit, viscous fingering via deformation of the elastic boundary [78]. For a fixed cell configuration, the interface goes from stable to unstable when the injection rate overcomes a critical threshold. The critical flow rate at which the interface destabilizes

increases with increasing initial gap thickness and decreases with increasing bending stiffness of the membrane [78]. In addition, it has been shown that the fingers grow faster with an increasing membrane thickness (i.e., lower deformability). Several studies of the same topic focused on the mechanisms of the stabilization under elastic membrane with theoretical and numerical considerations [75, 79, 80, 81]. The consideration of a theoretical model coupling the Föppl-von Kármán equations, which describe the elastic wall deformation, with Navier-Stokes equations or the lubrication theory showed good agreement and described well the experimental observations [81]. The axisymmetric inflation of the elastic sheet decreases the growth rate of the displacing fluid and the interface propagates into a narrower gap, which affects the classic destabilization mechanisms and enables stable displacements [75].

B. Using a tapered plate

Introducing a depth gradient in the flow cell can significantly modify the stability of the displacing interface and the "printer's instability" [12, 13, 16] is a good example. The printer's instability is manifested in coating flows when a viscous liquid is confined between a roller and a plane or between two rollers, and displaces air. The interface can present ribbing lines and be uneven when the pressure gradient over the meniscus is negative and large enough due to the rollers divergence [16]. A stability diagram revealed that the critical capillary number at which the flow becomes unstable increases with an increasing diverging angle [12, 13, 16].

These observations inspired numerous studies, and the impact of depth gradients in modified Hele–Shaw cells has since been investigated to a further extent [82, 83, 84, 85, 86, 87, 88, 89, 90]. An early experimental work coupled to a linear stability analysis [84] investigated the motion of immiscible, viscous fingers through a rectangular, tapered channel. When the viscous fingering problem takes place in a rectangular, tapered channel which has an increasing gap thickness in the flow direction (i.e., the cell is said to be diverging), the finger obtained presents a flatter tip than those found in flat cells, and will more likely become unstable [84]. On the other hand, when a finger propagates in a cell which is converging in

the flow direction (i.e., negative gap gradient), the tip of the finger is sharper than the ones observed in flat cells and the finger is more stable. These results of the pattern morphology can also be predicted by perturbative-theory models [82, 85]. The theoretical model for a semi-infinite bubble advancing into a converging channel revealed that the thickness of the film of the displacing fluid deposited on the walls increases with an increasing Ca and increasing α [82]. More recently, an experimental study coupled to a linear stability analysis [86] revealed for the first time the possible, total suppression of viscous fingering in rectangular tapered cells, using a negative gap gradient [86]. Remarkably, in a converging channel, the researchers observed the interface front goes from flat for a range of low values of Ca to finger-like for values of Ca bigger than a critical threshold. The theoretical model predicted the criterion for the stability transition to occur and showed pretty good agreement with the experiments for the range of depth gradient explored [86]. A linear stability analysis [87] and some numerical simulations [88, 89] also revealed the existence of the two distinct regimes in radial flows, with a transition that depends on the gap gradient, α, and the capillary number, Ca. Numerical simulations of the viscous fingering problem using a tilted, converging channel where gravitation is present, showed the transition between stable and unstable displacements [90]. Their results revealed that the onset of instabilities decreases with an increasing capillary number, Ca, and increasing Bond number, Bo.

1.5 Overview of the thesis

The primary objective of this thesis work is to give a better insight and understanding of the viscous fingering phenomenon in simplified heterogeneous porous media of modified Hele–Shaw cells, using both Newtonian and suspension fluids. Our work focused on experimental approach since there are relatively few experimental investigations regarding viscous fingering problems in tapered cells. The first study investigates the control and mechanism of viscously-unfavorable fluid-fluid displacements of immiscible fluids in novel radially tapered Hele–Shaw cells with Newtonian fluids. We analyze the flow stability diagram of the viscous fingering instability depending on the flow rate, depth gradient, and gap thickness.

Then, we investigated the displacement of suspensions in tapered flow cells to understand the impact of the particles on the pattern formation of viscous fingering. The combination of both stabilizing and destabilizing effects via the depth gradient and the particles, respectively, was studied. An interfacial stability analysis including the particle concentration was reported.

Chapter 2

Manipulation of viscous fingering in a radially-tapered cell geometry[1]

2.1 Introduction

Viscous fingering instabilities can be beneficial or detrimental depending upon the application. However, the control of viscous fingering has been a great challenge and hence investigated to a less extent since the mobility or viscosity contrast is often predetermined by the fluids chosen for the applications. Recently, such control has been achieved by controlling the injection rate of the displacing fluid [70, 76, 83], or using an upper elastic membrane forming a Hele-Shaw cell [75, 78, 79, 80]. In addition, a study has experimentally demonstrated the feasibility of suppressing fingering via a capillary effect using a rectangular Hele-Shaw cell with a converging gap [86], which has attracted renewed interest in the topic [64, 88, 89, 91, 92, 93, 94]. Subsequently, several potential strategies for controlling viscous fingering instability have been explored, for instance, via wettability control of the

[1]The material presented in this chapter is based on Bongrand, G. and Tsai, P.A., "Manipulation of viscous fingering in a radially tapered cell geometry." Physical Review E, Rapid Communications, 97(6), 061101, 2018.

fluids [67, 68], by experimentally lifting a plate with a time-dependent strategy at fixed flow rates [74] and numerically exploiting a gravitational (Rayleigh-Taylor) instability [90]. Nonetheless, systematic and thorough experimental investigation has yet to be carried out on the effect of depth gradients in a radial injection. In this chapter, we experimentally investigate viscous fingering problem in radial tapered Hele–Shaw cells (see Fig. 2.1) and examine the impacts of depth gradients, radial propagation, and flow rates.

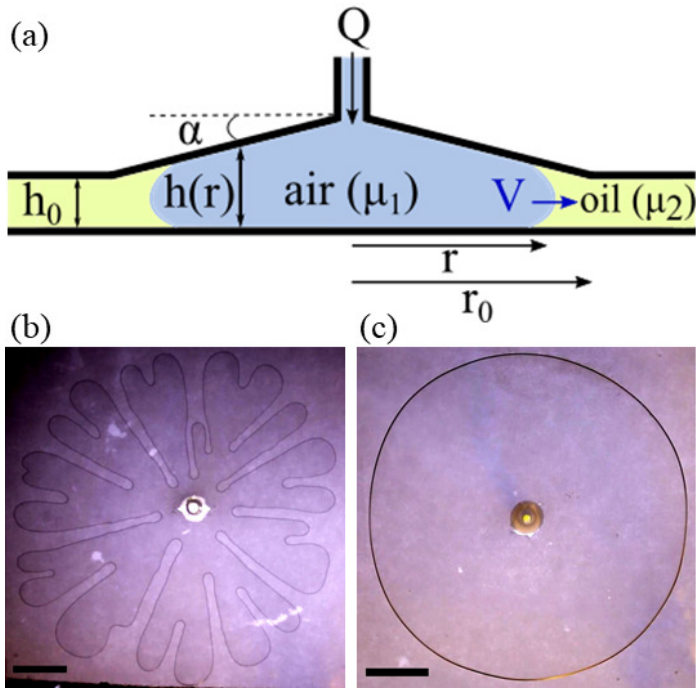

Figure 2.1: (a) Schematic diagram of the side view of the experimental setup of immiscible fluid-fluid displacement in a radially converging passage, with a viscosity ratio $\lambda = \mu_2/\mu_1 = 8.8 \times 10^3$. (b) Snapshot of a classical viscous-fingering pattern obtained when air pushes oil in a flat radial Hele–Shaw cell with $h_0 = 1.2$ mm and $Q = 40$ mL/min. (c) In contrast, snapshot of a stable interface with a complete sweep of oil by air in a radially tapered cell with $\alpha = -6.67 \times 10^{-2}$, $h_0 = 150$ μm, and $Q = 40$ mL/min. For the experiments in (b) and (c), h_0 are chosen so that both configurations have equal fluid volumes. The scale bars in (b) and (c) are 2 cm.

2.2 Experimental setup and procedure

In our experiments, a variant of a Hele–Shaw cell with a converging gap is used to control the fingering instability with a radial injection (shown in Fig. 2.1(a)). The bottom plate is made of plexiglass and strengthened by another, thicker plate to avoid any bending. The upper plate is tapered over a radius r_0 = 7cm, with a negative gap gradient, $\alpha = dh(r)/dr$, i.e., the ratio of the height to length of the tapered area. We manufactured the tapered plate made of clear photopolymer resin using a 3D printer with an accuracy of 25 μm, and use some fine sand paper to remove the eventual small roughnesses. The accuracy of the gap gradients has been checked for each plate along four different radial directions by measuring the decrease in height every centimeter, and the value of α reported in our study was the average of the four measurements. We control the height of the outer flat edge h_0, using translation stages with an accuracy of 10 μm. The gap thickness inside the cell evolves linearly along the radius $h(r) = h_0 + \alpha(r - r_0)$, i.e., $\alpha = \frac{h_0 - h(0)}{r_0} < 0$. The defending fluid is heavy mineral oil (viscosity μ_2 =158 cP, Fisher Scientific), which initially is injected into and fully saturates the cell. We then inject air (viscosity $\mu_1 = 1.8 \times 10^{-5}$ Pa.s = 0.018 cP) via a syringe pump at a constant flow rate Q, ranging from 10 mL/min to 300 mL/min with an accuracy of 0.05%. The contact angles of the heavy mineral oil on the plexiglass and on the 3D printed plate have been measured to be 21.6 ° and 14.2 °, respectively.

The observations are captured with a camera (Canon EOS 70D) at 30 fps (frames per second), and we use backlighting to enhance the contrast of visualization. We use ImageJ and Matlab to analyze the images and track the evolution of the interface. The local velocity, V, is calculated by tracking the interface position ($R(t)$) varying in time (over a short period of time) and estimated with the slope of $R(t)$, i.e., $dR(t)/dt$. The velocity measurements reported for experiments showing transitional behaviours have been performed on symmetric displacements and checked for at least two different radial directions. The way of defining the stability of the interface is based on whether the interface perturbation grows in time, i.e., the growth rate of the perturbation is larger than zero. The corresponding experimental evidence of a viscous fingering instability is manifested in a growing wavy

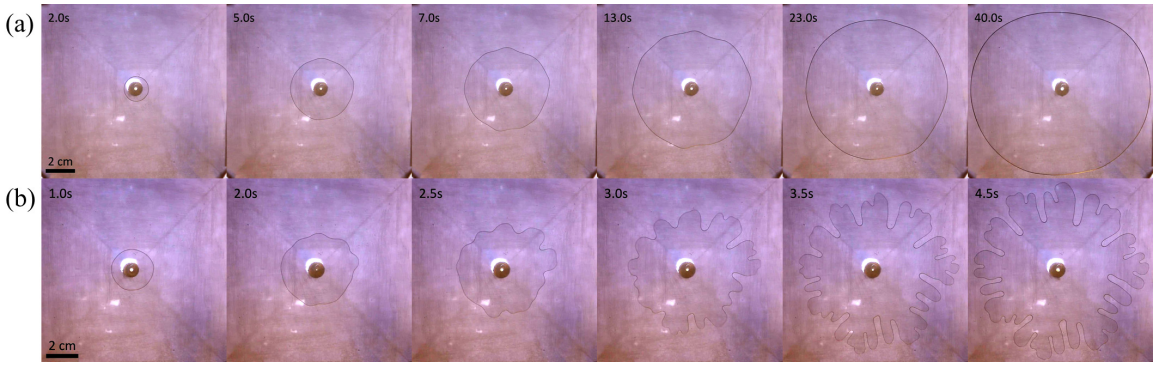

Figure 2.2: The dependence of sweep efficiency on flow rate Q: snapshots of two representative experiments of air displacing oil for the same geometrical configuration with the gap gradient $\alpha = -4.75 \times 10^{-2}$ and $h_0 = 500\ \mu m$, but different flow rates: (a) stable displacement at $Q = 40$ mL/min, whereas (b) viscous fingering at $Q = 110$ mL/min.

profile of the fluid-fluid interface.

We characterize the importance of the viscous forces relative to capillary forces using the capillary number, $Ca = 12\mu_2 V/\gamma$, where the surface tension of the oil, $\gamma = 30$ mN/m, was measured using a tensiometer. The fluid combination in our experiments has a viscosity ratio of $\lambda = \mu_2/\mu_1 = 8.8 \times 10^3$. The values of the Reynolds number in our experiments were in the range $10^{-2} - 10^{-1}$, and the values of the Bond number were in the range $10^{-1} - 10^{0}$.

2.3 Results and discussions

We first performed control experiments in flat and tapered cells, set with respective gap thicknesses so that both geometries have equivalent fluid volumes. As in the case of the classical Saffman-Taylor instability, when we conducted experiments with unfavorable viscosity-ratio displacement ($\mu_1 < \mu_2$) in a uniform cell, we observed unstable interfacial propagation with fingering, as shown in Fig. 2.1(b). However, remarkably, when we carry out a similar experiment with $\mu_1 < \mu_2$ in a converging cell, the interface can be stabilized, as illustrated in Fig. 2.1(c). The results obtained for a uniform Hele–Shaw cell here are qualitatively consistent (in spite of different tip-splitting patterns) with the results shown in [30] performed for $h_0 = 1.5$ mm, $Q \approx 80$ ml/min, and $\gamma = 63$ mN/m.

Through our experiments, we aim to understand the variation of the onset of instabilities

for various flow configurations with different α. By systematically varying the flow rate, Q (for a fixed α and h_0), we observed a stable interface at low Q throughout the experiment (see Fig. 2.2(a)). However, above a certain flow rate, the interface becomes wavy, and the instability grows as air displaces the oil, as shown in Fig. 2.2(b). Physically, in the case of $\lambda > 1$, the viscous pressure gradient gained is $\Delta P_\nu \sim \frac{\mu}{k} V$ and further destabilizes the interface as fluid travels radially outwards. For the radial injection, the interfacial velocity can significantly change due to mass conservation via a radially increasing cross-sectional area and a decreasing gap thickness, and hence alters ΔP_ν. On the other hand, the converging gap introduces a varying capillary pressure, $\Delta P_\gamma \sim \frac{2\gamma}{h(r)}$, which increases and plays a crucial role in stabilizing the interface when fluids travel in a passage of decreasing depth.

By varying Q gradually for different α, we characterize the critical threshold of flow rate, Q_c, between stable (Fig. 2.3(b)) and unstable (Fig. 2.3(c)) displacements. Figure 2.3(a) illustrates the phase diagram of stable *vs.* unstable interfacial propagation for different α and Q. This stability diagram reveals a general trend of increasing Q_c with an increasing depth gradient, $|\alpha|$.

Based on linear stability analysis, a theoretical model to characterize the interface behaviour has been carried out for a rectangular [86] or radial fluid cell [87]. The stability of a radially tapered viscous fingering interface is expressed in terms of its growth rate, σ [87]:

$$\frac{r\sigma}{V} = -(1 + \frac{\alpha r}{h}) + (1 + \frac{2\alpha + (h/r)^2}{Ca})N - \frac{(h/r)^2}{Ca}N^3, \tag{2.1}$$

where N is the number of fingers, and r is the radial position of the interface. $\sigma < 0$ characterizes a stable interface, while the critical transition occurs when $\sigma = 0$. We extract the values of r, N and V from the experiments showing the transitional behaviour from a stable to an unstable interface to analyze the growth rates. Under a constant flow rate, Q, as the fluid interface advances radially, $r = r(t)$, the interfacial speed V changes due to mass conservation, i.e., $V = V(r(t))$. Consequently, the capillary number varies greatly with r. For a gas displacing a wetting viscous liquid in a rectangular cell, the stability of the interface depends only on Ca and α, with a stable interface when $1 + 2\alpha/Ca < 0$ [86]. On

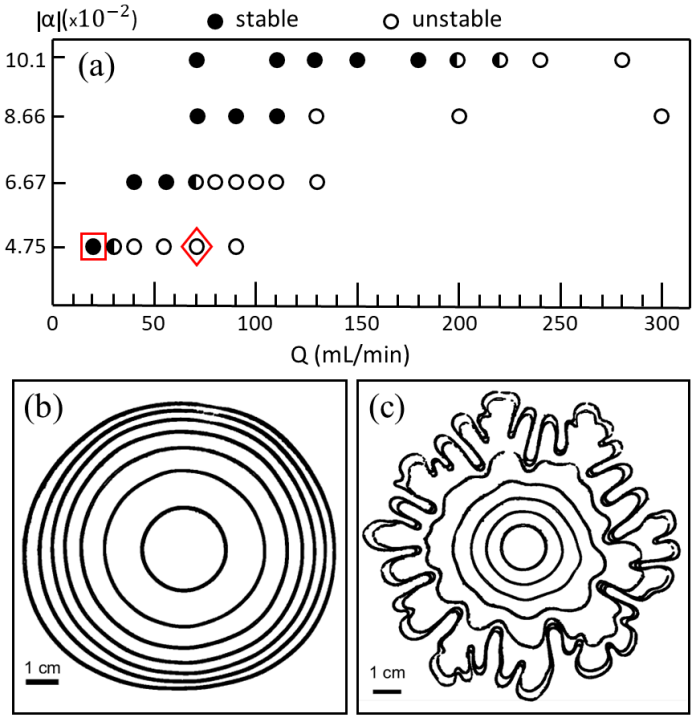

Figure 2.3: (a) Stability diagram of stable *vs.* unstable propagation front by varying the flow rate Q, for different gap gradients α (while $h_0 = 250\ \mu m$). The general trend shows that for each α, stable and complete sweep occurs at a relatively small Q (denoted by $\bullet$), whereas unstable fingering propagation emerges at large Q ($\circ$). Each data point here has been reproduced $3-5$ times. For a radially-tapered cell of $\alpha = -4.75 \times 10^{-2}$, $h_0 = 250\ \mu$m, time-evolution of top-view, stable interfaces with $Q = 20$ mL/min in (b) (corresponding to $\square$ in (a)), while unstable interfaces in (c) for $Q = 70$ mL/min ($\diamond$ in (a)). The time steps are $\Delta t = 9$ s and 1 s between each contours for (b) and (c), respectively.

the other hand, the linear stability problem and the resulting growth rate, σ, for a radial variant Hele–Shaw cell are more complex than those in a rectangular configuration, due to the interplay between geometric and capillary parameters (e.g. r, Ca, and N).

To further compare our experimental results with the analytical prediction, we analyze in Fig. 2.4 the influence of r and N at the transition on the growth rate of viscous fingering for our experimental conditions. To do so, we measured the parameters r, N and V at the transition point, when the wavy and fingering interface starts to set in, by directly analyzing from our captured videos (for each α and h_0). Figure 2.4(a) shows the variation of the theoretical growth rate σ with respect to r (depicted by the open symbols), using Eq. 2.1,

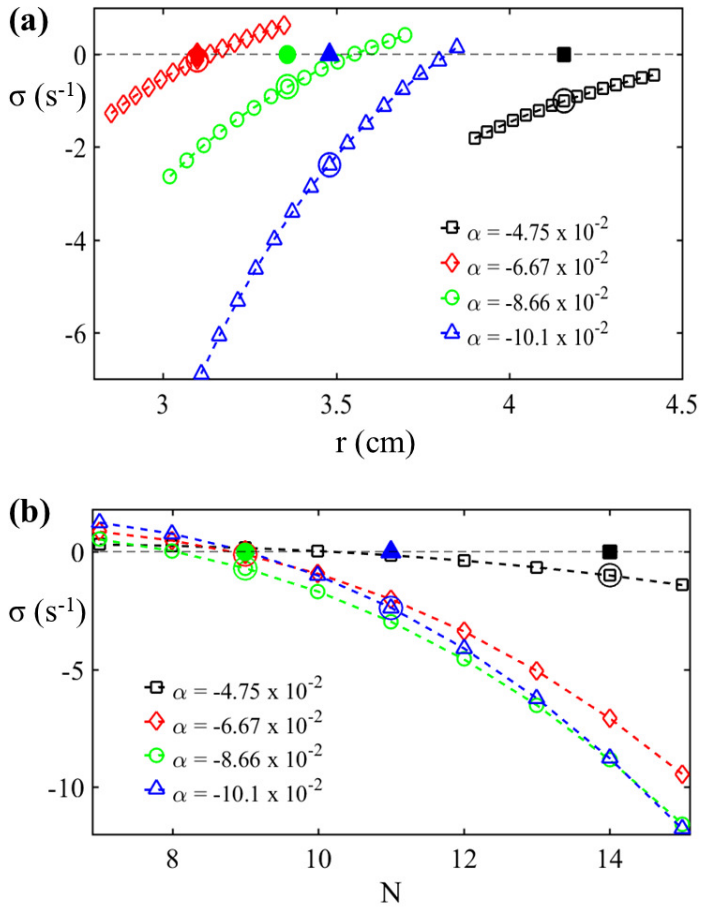

Figure 2.4: (a) The dependence of the growth rate σ on the radial position r, based on a linear stability analysis [87], while V and N are extracted from our experiments when unstable fingering and transition occur for h_0 = 250 μm for different α. (b) Similarly, the change of σ with the number of fingers, N, while V and r are extracted from our experimental results. The open circles in both (a) and (b) represent the theoretical values of the growth rate estimated using experimental r, N and V observed at the transition for different α. The filled markers (■, ♦, ●, ▲) correspond to the experimental critical values of r and N for (a) and (b) when $\sigma = 0$, respectively.

with N and V as input using our experimental values observed at the critical transition. For different α, we observed a strong dependence of growth rate on r for a certain critical fingering number N observed. As revealed in Fig. 2.4(a), within 1 cm, a stable interface can become unstable. For different α, our corresponding experimental data of critical transition observed are depicted with filled symbols, showing the empirical critical r at the transition, with $\sigma = 0$. For small $|\alpha|$, the experimental data agree well with the theoretical prediction.

For a relatively large $|\alpha|$, the experimental data show an earlier critical transition (i.e., a smaller critical radial position when $\sigma \approx 0$), while the theoretical analysis would predict a negative σ. Nevertheless, these comparisons show consistent results because the difference in critical r is within 0.5 cm.

Using a similar approach, Figure 2.4(b) reveals the impact of N on σ, predicted by the analytical linear stability analysis with r and V fixed using the experimental critical values. Overall, our experimental results are consistent with the analysis of the influences of r and N. We observe that the results for $\alpha = -6.67 \times 10^{-2}$, and $\alpha = -8.66 \times 10^{-2}$, agree well with the theoretical transition when $\sigma = 0$, while a deviation is observed for $\alpha = -4.75 \times 10^{-2}$, and $\alpha = -10.1 \times 10^{-2}$. Nevertheless, the theoretical prediction of growth rate can vary significantly over a small range of r and N. The theoretical model Eq. 2.1 [87] assumes a symmetric displacement, a constant static contact angle, and a small dimensionless depth variation, i.e., $\|\frac{\alpha r}{Nh}\| << 1$. In contrast, our experiments have this dimensionless parameter ranging from 5×10^{-2} to 10^{-1} and may have some surface roughness (due to the polish using fine sand papers) leading to inhomogeneous wetting and front propagation. These factors are likely the reasons for the deviation observed. Since multiple experimental parameters (e.g. Q, α, N and r) influence the growth rate of radial viscous fingering, we further analyze the critical Capillary number, Ca^*.

Figure 2.5(a) shows the comparison of experimentally observed Ca^* with the theoretical prediction Ca^*_{th} based on Eq. 2.1 at the transition (i.e, by setting $\sigma = 0$), where:

$$Ca^*_{th} = \frac{[2\alpha + (h/r)^2]N - (h/r)^2 N^3}{1 + (\alpha r/h) - N}. \tag{2.2}$$

The comparison, shown in Fig 2.5(a), reveal consistent results between the experimental and theoretical critical capillary numbers. The experimental capillary number values, Ca^*, are determined via $Ca = 12\mu_2 V/\gamma$ for each α and h_0, where the local velocity, V, is measured with the videos showing a transitional displacement from a stable to an unstable interface. The theoretical predictions of Ca^*_{th} are estimated using Eq. 2.2, with the inputs of N and average r analyzed from the same experimental videos.

Our experimental results show the small effect of h_0 on Ca^* (●, ■, ♦ in Fig. 2.5), while

the theoretical critical Ca^*_{th} from Eq. 2.2 depends on $h(r) = h_0 + \alpha(r - r_0)$. Overall, a good agreement is found for smaller gap gradient. More importantly, the general trend of both theoretical Ca^*_{th} and experimental Ca^* increases with an increasing magnitude of the gap gradient. In other words, a larger interfacial velocity is required to trigger viscous fingering instability in a steeply convergent gap, where large capillary pressure is present and acts to stabilize the interface. For relatively larger $|\alpha|$, the slight deviation may be explained with the experimental difficulty of meeting the theoretical assumptions mentioned before such

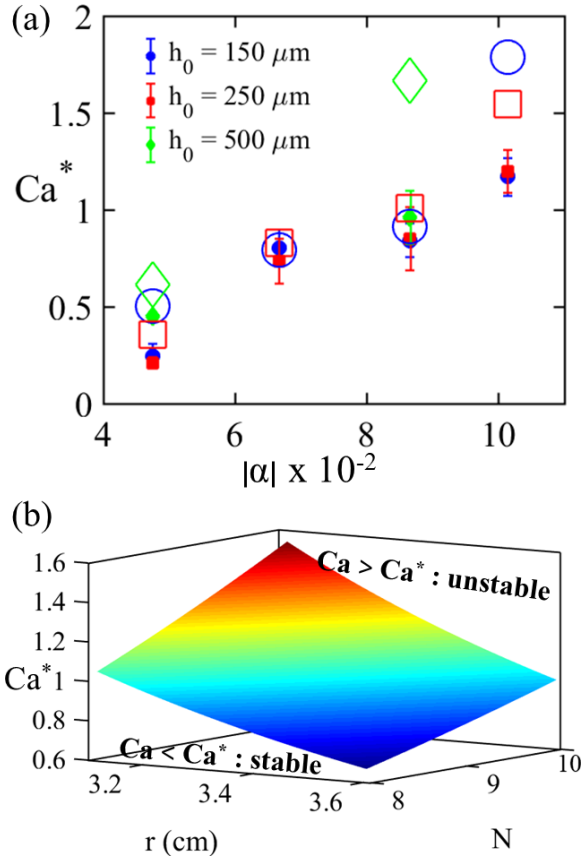

Figure 2.5: (a) Variation of the critical Capillary number Ca^* separating stable *vs* unstable displacements for different depth gradients α and h_0. We compare the experimental values (●, ■, ♦) to the theoretical Ca^*_{th} (○, □, ◊) derived from Eq. (2.2) with α, r and N from our experimental results and parameters. The error bars shown represent the standard deviation obtained from 4 – 6 different measurements (based on the results of radially symmetric displacement). (b) Surface plot of theoretical Ca^*_{th} greatly depends on r and N using Eq. (2.2), for $\alpha = -8.66 \times 10^{-2}$ and $h_0 = 250\ \mu m$, showing a stable displacement when $Ca < Ca^*$ whereas unstable one when $Ca > Ca^*$.

as symmetric displacement with constant static contact angle, no wetting film adhesive to the wall, and a small dimensionless depth variation. In addition, the strong dependence of theoretical Ca^*_{th} based on Eq. 2.2 on r and N is shown in Fig. 2.5(b). For instance, within a range of 0.5 cm in r and $N \pm 1$, Ca^*_{th} varies from 0.67 to 1.54 for the specific configuration presented in Fig. 2.5(b). This drastic change within such a small radial position, r, and/or number of fingers, N, may explain the slight and moderate deviations observed for relatively moderate $|\alpha|$ in Fig. 2.5(a).

2.4 Conclusions

In summary, we have experimentally demonstrated that the presence of a radial depth gradient (i.e., permeability variation), can alter significantly the viscous fingering instability and pattern. Using a converging passage, the classic viscous fingering commonly observed in a flat Hele–Shaw cell can be completely suppressed with a suitable flow rate. For each converging gradient, α, we can tune the viscous-fingering instability from a stable to an unstable displacement by increasing the flow rate Q injected. This critical flow rate is increased for a steeper gap gradient. We further compare our experimental results with a theoretical linear stability analysis, showing consistent dependence of the instability growth rate on radial location r and N. From the experimental results with different α, we further showed that the critical threshold Ca^* increases with an increasing gap gradient $|\alpha|$, in good agreement with a recent theoretical prediction considering the effect of capillary pressure [87]. Our experimental results reveal for the first time the possibility of controlling interfacial instabilities with a radial injection in an inhomogeneous passage. The results of critical Ca^* depending on α, r, h_0 and N are beneficial for the design and prediction of flow settings where the process of fluid-fluid displacement in a porous medium is crucial.

Chapter 3

Control of viscous fingering of suspensions using a tapered cell

3.1 Introduction

Complex fluids differ significantly from Newtonian fluids in their rheological features, with varying viscosity effects such as shear-thickening/thinning, yield stress and elastic behaviours [46]. Due to the increasing use of complex fluids in various applications, interfacial instabilities occurring in those have been recently attracting more and more attention. The problem of viscous fingering of complex fluids in Hele–Shaw cells have been investigated to an extent with fluids such as polymers [47, 48, 50, 54, 55], gels [51, 52, 53], surfactants [47, 49], foams [51, 95], emulsions [58, 96], liquid crystals [97] or suspensions [56, 57, 59, 60, 98, 99]. The complexity of such fluid systems induces a wider variety of morphological pattern formations, such as side-branching, fracture-like or snowflake-like patterns.

Suspensions with solid grains, crystal particles or materials are often encountered when fluids flow through rock fractures or other high-permeability media. The presence of particles provides a means to modify fluid-fluid interfaces. The additional minute particles can either stabilize or destabilize the interfaces depending on the applications. For instance,

particles can accumulate onto the interface and strengthen it against instabilities by forming dense monolayers [100, 101, 102], which can be used to stabilize emulsions [103]. In other systems, particles entrained in a fluid flow can also alter the dynamics of the interface with the example of the accelerated droplet pinch-off once immersed in a viscous suspension [104, 105]. Hence, tuning interfacial instabilities in viscous fingering applications with particles is possible. The inverse Saffman-Taylor problem of a less viscous fluid displaced by another more viscous one, where particles are suspended, can destabilize the particle band and form fingering patterns [61, 62, 63, 64]. Nevertheless, the displacement of a more viscous suspension or a granular mixture by a less viscous Newtonian fluid in Hele–Shaw cells often leads to more unstable and complex interfaces with possible occurrence of side-branched [59] and crack-like patterns [57], or frictional fingers [98, 99]. Also, some studies about the Saffman-Taylor problem pushing a suspension revealed that the onset of viscous fingering instabilities decreases with an increasing particle concentration [56, 60].

An efficient technique to control the viscous fingering instabilities has been shown to be the modification of the cell geometry by the introduction of an elastic membrane [75, 78, 79, 81] or a converging tapered plate [86, 87, 89, 106]. Inspired by these observations, we study the stability of fluid-fluid displacements combining the stabilizing effect of the radial converging depth gradient with the destabilizing effect due to the particles suspended in the more viscous, displaced fluid. In this study, we experimentally examine for the first time the impacts of the injection pressure of displacing gas, depth gradients, and particle concentrations on the stability of the interface during a classical viscous fingering displacement.

3.2 Experimental setup and procedure

In our experiments, a converging cell geometry—similar to a Hele–Shaw cell of two parallel plates but with an upper plate tapered—is used to control the fingering instability in a radial injection (see in Fig. 3.1(a)). The tapered top-plate is made of PMMA while the bottom of a glass, and both plates are thick to avoid any bending. The upper plate is tapered over

a radius range of r_0 = 14 cm, with a varying gap thickness $h(r)$. The latter evolves linearly along the cell radius, i.e., $h(r) = h_0 + \alpha(r - r_0)$, and the outer flat edge height h_0 is set via threaded studs and fixed to be 500 μm, with an accuracy of 25 μm. Hence, a critical control parameter is the gap gradient, $\alpha = dh(r)/dr$, i.e., the ratio of the height to length of the tapered area; here, α is negative for the converging cells used in the experiments.

The suspension is prepared by mixing a solution of glycerol with 15.3 $vol\%$ of water (of viscosity μ_2 = 146 cP and density $\rho \approx 1.23$ g/cm^3) with neutrally-buoyant polyethylene particles (density ρ = 1.20 g/cm^3, Cospheric) of a particle diameter range D = 106–125 μm. The amount of particle present in the suspension is characterized by the particle concentration, c_p, expressed in weight percent ($wt\%$) of the total solution. Instead of injecting the suspension, the defending fluid is present in a liquid bath confined by the bottom, reservoir container. Then, the upper plate is lowered into the liquid bath, and the suspension saturates the cell. This technique is used to obtain a random particle distribution. Once the suspension fluid is set, we then inject the nitrogen N_2 (of viscosity $\mu_1 = 1.76 \times 10^{-5}$ Pa.s = 0.0176 cP) at a constant injection pressure, p, ranging from about 0.08 psi to 3.3 psi by a pressure gauge with an accuracy of 0.05 psi.

The corresponding flow rates using a pressure regulator have been estimated to be in the order of 1 L/min. For instance, a gas injection at 1.1 psi has been estimated to be equivalent to a flow rate $Q \approx 5$ L/min.

The experiments are recorded using a camera (Canon EOS 70D) at a frame rate of 60 fps (frames per second) with backlighting to enhance the contrast of visualization. We perform post-processing and analysis on the images to track the interface profiles using ImageJ and

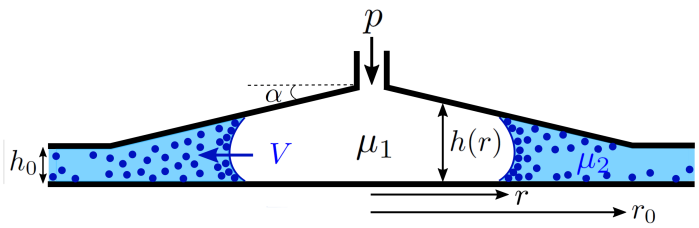

Figure 3.1: Schematic diagram of the side view of the experimental setup of displacement of a suspension by nitrogen (N_2) in a radially converging passage with r_0 = 14 cm.

Table 3.1: Table of the change of the viscosity μ_2 with the particle concentration c_p. The viscosity was measured via a rheometer, right after mixing the suspension solutions.

Particle concentration c_p ($wt\%$)	Viscosity (cP)
0	146
1	157
2.5	160
5	170

Matlab. The local velocity, V, is measured by capturing the evolution of the interfacial position over a short period and calculated with the slope, $dR(t)/dt$. The surface tension of the water-glycerol mixture is about $\gamma = 64.8$ mN/m [107] and is assumed constant for different c_p. The contact angles of the water-glycerol solution on the PMMA and glass surfaces have been measured to be 68.6 ° and 62.2 °, respectively. Some rheological measurements with a concentric cylinder cell have been performed to know how the viscosity μ_2 of the displaced fluid varies depending on c_p (see Fig. 3.1(b)). Surprisingly, the measurement results of the suspensions used showed no shear-thickening effects but closely follow Newton's linear relation between μ and the shear stress. However, a surprising decrease in μ_2 was measured after the viscous fingering experiments. A more-detailed description of these observations, measurements and comments, is given in Appendix A. The values of the Reynolds number in our experiments were of the order of magnitude $10^{-1} - 10^{0}$, and the values of the Bond number were in the order of magnitude $10^{-1} - 10^{0}$.

3.3 Results and discussions

Through our experiments, we aim to understand the impact of the suspended particles in the displaced fluid on the onset of instabilities, for various depth gradients, α, and particle concentrations, c_p ($wt\%$). We first performed a set of control experiments with N_2 pushing the pure water-glycerol solution (i.e., $c_p = 0$ $wt\%$) as a reference to compare with the results in suspensions. For the flat Hele–Shaw cell ($\alpha = 0$), we set $h_0 = 2.7$ mm so that the fluid volume is similar to the cell geometry for $\alpha = -5.36 \times 10^{-2}$, the most stable situation. As

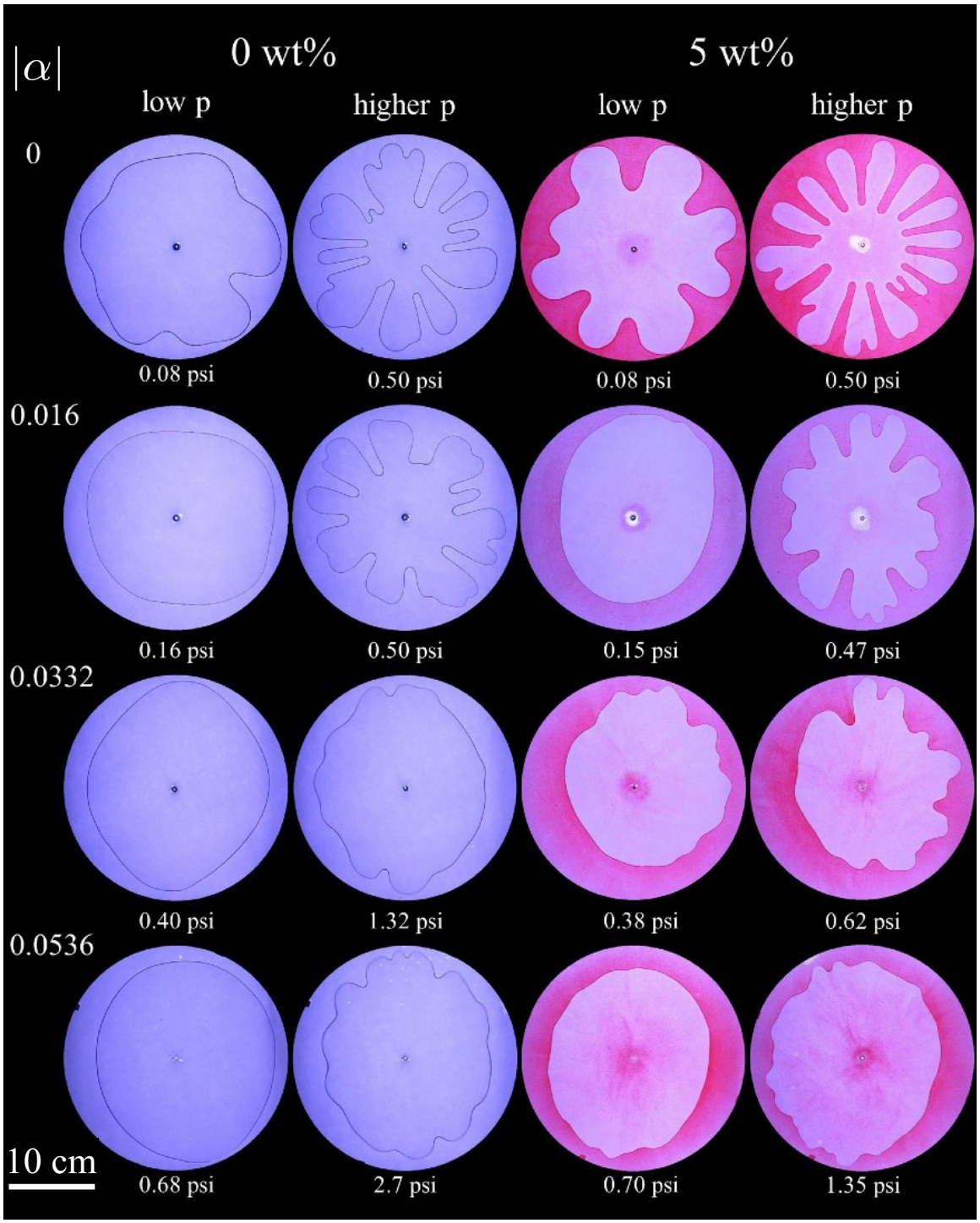

Figure 3.2: The dependence of sweep efficiency on injection pressure, p, for different depth gradient, α, and particle concentration, c_p. Snapshots of representative patterns obtained when N_2 pushes water-glycerol solutions with or without micro-particles. Globally, the extraction of the displaced fluid was increased with an increasing $|\alpha|$ but decreased with the presence of particles. For the tapered cells h_0 = 500 μm, whereas h_0 = 2.7 mm for the flat cell so that the cells would have the same fluid volume as for $\alpha = -5.36 \times 10^{-2}$. The length bar is 10 cm.

shown in Fig. 3.2, we observed the destabilization of the interface in a flat Hele–Shaw cell, as expected for the case of classical viscous fingering. For a Newtonian system of fluids, Figure 3.2 reveals that the sweep efficiency increases with a steeper gap gradient and decreases with an increasing injection pressure. For example, for $c_p = 0$ $wt\%$, the late interface profile for $\alpha = -1.6 \times 10^{-2}$ and $p = 0.50$ psi presents well-developed viscous fingers, whereas an almost-rounded interface is captured for $\alpha = -5.36 \times 10^{-2}$ and $p = 0.68$ psi. The same general trend was found for a displaced suspension of concentration $c_p = 5$ $wt\%$. Nevertheless, the presence of particles seems to decrease the sweep efficiency. Remarkably, experiments that led to a full sweep with Newtonian fluids now present unstable interface profiles when particles are introduced in the displacing fluid (see Fig. 3.2). In addition, for the same cell geometry, smaller extraction efficiency is obtained for $c_p = 5$ $wt\%$ at a certain p than when $c_p = 0$ $wt\%$ at a higher p.

Although the mechanism of particles on the viscous fingering pattern formation is not fully well-understood, it seems that the suspensions have a destabilizing effect on the viscous fingering interfaces, when they get displaced. According to Tab. 3.1 and other studies using particles [56, 60], it seems the effective viscosity may be increased with an increase in c_p, which would lead to an increased viscosity ratio λ and could be an explanation for the destabilizing effect by the particles. Moreover, as the interface advances, the meniscus captures some particles that accumulate on it [108]. Hence, c_p is increased locally close to the interface, so is the local viscosity ratio, which could lead to interfacial destabilization at lower p.

For a fixed α and c_p, we increase systematically the injection pressure, p, and observe stable interfaces at low p whereas viscous fingering occurs at higher p, as illustrated in Fig. 3.2. We systematically vary α and c_p and establish a stability diagram to quantify this critical pressure threshold between stable *vs.* unstable displacement (see Fig. 3.3).

The stability diagram of Fig. 3.3 reveals a global trend of increasing critical injection pressure, $p^\star$, with an increasing depth gradient, $|\alpha|$, but decreasing $p^\star$ with an increasing c_p. Some similar results were found for Newtonian fluids in [106], with an increasing critical

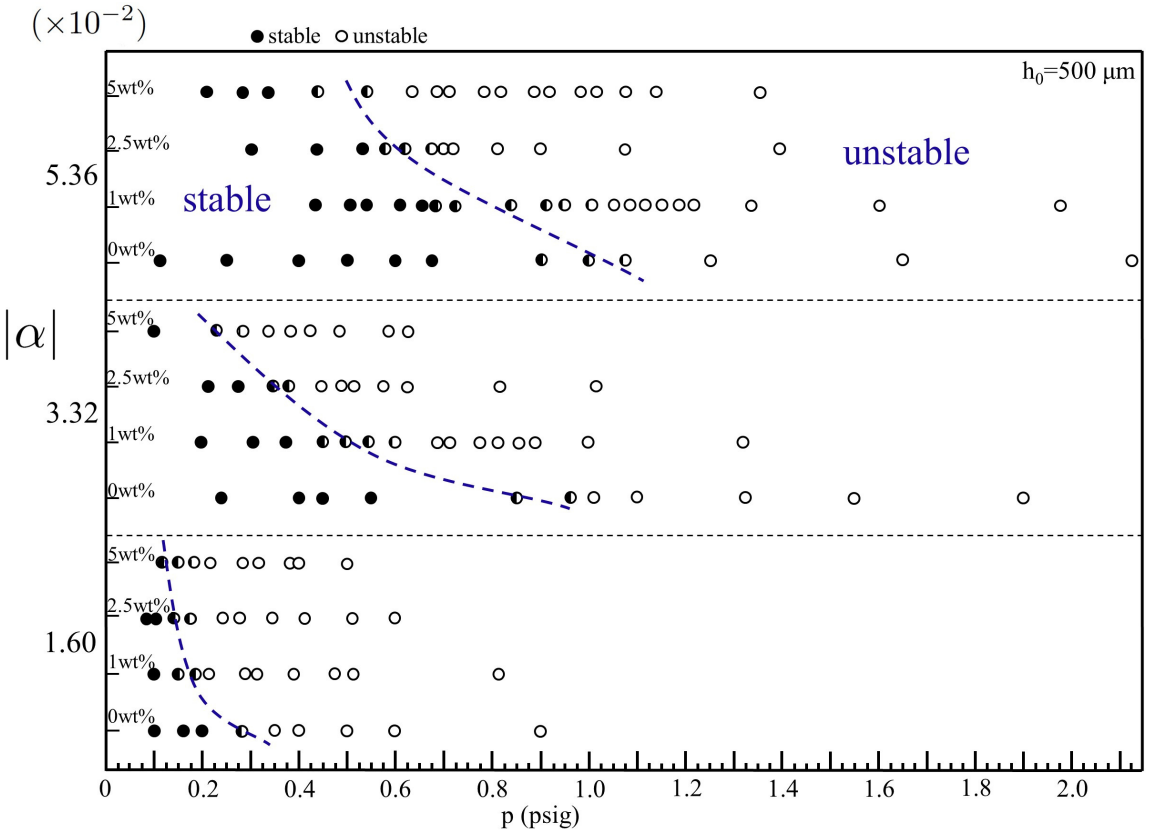

Figure 3.3: Stability diagram of stable *vs.* unstable displacements by varying the injection pressure p, for different gap gradients, α, and particle concentrations c_p (while h_0 = 500 μm). The general trend shows that for each α, stable and complete sweep occurs at a relatively small p (denoted by $\bullet$), whereas unstable fingering propagation emerges at larger p ($\circ$). The threshold (highlighted by the dashed lines) moves towards lower p as c_p increases or $|\alpha|$ decreases. Each data point has been checked with reproduced results using at least three different experiments.

flow rate threshold for steeper gradients. For $\alpha = -1.60 \times 10^{-2}$ and $\alpha = -3.32 \times 10^{-2}$, the drop in the critical pressure from the Newtonian case (i.e., c_p = 0 $wt\%$) to the slightly concentrated suspensions is quite significant, whereas a gradual decrease is observed while moving towards higher particle concentrations. For $\alpha = -5.36 \times 10^{-2}$, the variation of p^* seems more linear with an increasing c_p.

Figure 3.4 shows the time-elapsed interface profiles between the low and high pressures used, for different α and c_p. We observe the evolution of more rounded and symmetric interfaces at low p, leading to a full sweep of the displaced fluid. On the other hand, as

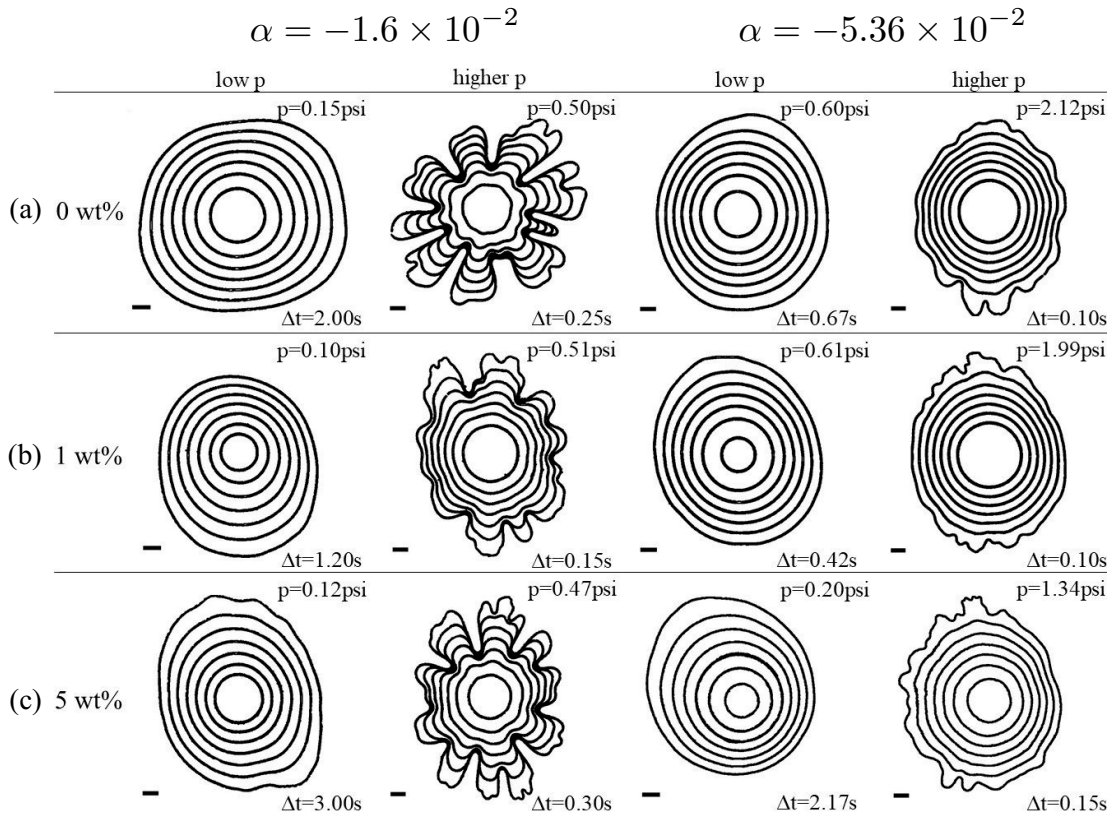

Figure 3.4: Top-view time-evolution of stable *vs.* unstable interface profiles illustrating the difference in stability depending on the injection pressure, p, for different configurations (α, $wt\%$) at h_0 = 500 μm. The time steps between two consecutive interfaces are specified for each situation, and the scale bars are 2 cm.

p is increased a manifestation of viscous fingering with partial sweep, and secondary nonlinear instabilities, e.g., tip-splitting (mainly) and sometimes side-branching, are obtained. Remarkably, we notice that the number of fingers remains constant after the destabilization of the interface, except the tip-splitting phenomena. For $\alpha = -1.6 \times 10^{-2}$ and for a similar magnitude of p, from analyzing videos where viscous fingering instabilities are well developed, the number of fingers when instabilities start to appear seems to remain almost constant with a varying c_p. For instance, for $\alpha = -1.6 \times 10^{-2}$ and $p \sim 0.5$ psi, we found the number of fingers, N, to be almost constant at a value of $N \sim 8$ for different c_p (see Fig.3.4). In addition, the results in Fig. 3.4 indicate the difficulty of obtaining highly sym-

metric displacements since the process is sensitive to different factors such as the outer gap thickness, h_0, the cell's leveling, the surface roughness, and the uniformity of the particle distribution. By repeating the same procedure for the runs showing transitional behaviour when fingering starts to set in, we can extract the local interfacial velocity, V, and then define a critical velocity, V^*, for each different configurations of α and c_p.

Figure 3.5(a) shows the variation of the critical pressure p^*, separating stable displacements from unstable ones (cf Fig. 3.3) depending on α and c_p. For a fixed particle concentration, c_p, the critical pressure increases with a steeper gap gradient. When the fluids travel radially outwards, the converging gap gradient results in a capillary pressure gradient, Δp_γ, which increases and helps towards stabilizing the interface. On the other hand, the injection pressure of the gas, p, acts against the capillary pressure and destabilizes the interface. As a result, as Δp_γ increases with an increasing $|\alpha|$, the trend of increasing p^* for a steeper gradient seems coherent. For a fixed α, we show that p^* decreases with an increasing c_p. One possible explanation for the decreasing trend of p^* with c_p could be an increase in the local viscosity ratio. As the interface propagates radially, particles are captured by the interface and the particle concentration is locally increased. The viscosity of the suspension solutions is thought to increase with an increasing c_p, which would result in a local increase of the viscosity ratio close to the interface. For low values of α, we observe an offset in the values of critical pressure between experiments with suspensions ($c_p \geq 1$ $wt\%$) and Newtonian solutions ($c_p = 0$ $wt\%$). However, for $\alpha = -5.36 \times 10^{-2}$, the gap in p^* happens between $c_p \geq 2.5$ $wt\%$ and $c_p \leq 1$ $wt\%$, as shown in Fig. 3.5(a). The significant differences in p^* between the displacements of solutions and suspensions reveal the destabilizing effect of the particles on the propagation front. Furthermore, we notice the values of p^* are closer for the lower value of α than those for steeper gradients. In other words, the slope of $p^*(\alpha, c_p)$ for a fixed c_p (i.e., $\frac{dp^*(c_p)}{d\alpha}$) increases with an increasing particle concentration, c_p (see Fig. 3.5(a)). Therefore, our experimental results imply that the denser is the suspension, the more important is the destabilizing effect of the particles or, the more reduced is the stabilizing effect of the gap gradient. The presence of the particles

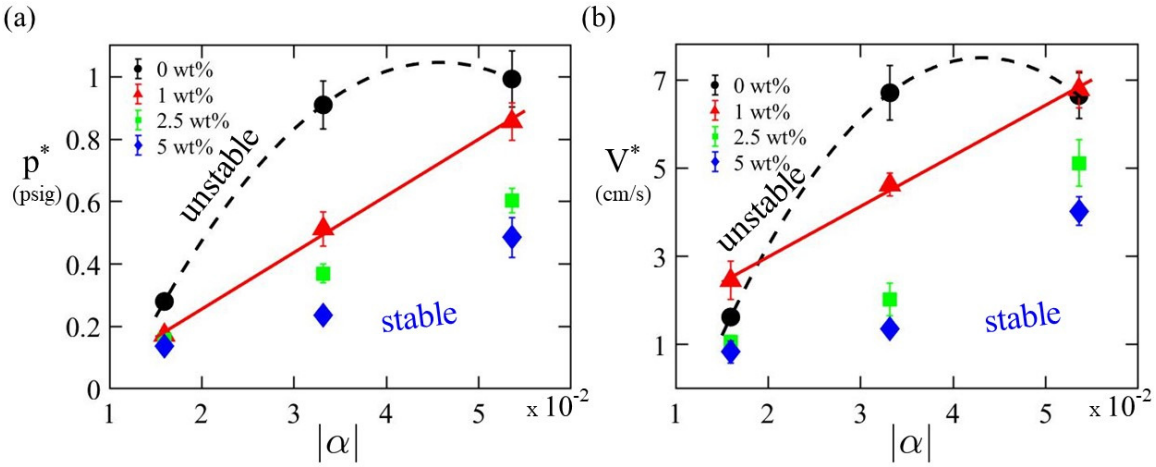

Figure 3.5: Variation of the experimental results of critical injection pressure (p^*) in (a) and interfacial velocity (V^*) in (b), separating stable *vs* unstable displacements for different depth gradients α and c_p. Each data represents the average values obtained from 3–4 different measurements, and the error bars show the corresponding standard deviation. The dashed, black lines separate stable from unstable displacements for the Newtonian cases (i.e., c_p = 0 $wt\%$) whereas the full, red lines highlight the transition for suspension solutions (i.e., $c_p \geq 1$ $wt\%$). For c_p = 0 $wt\%$, as a reference, the dashed line represents a quadratic fitting based on the 3 data points. Ideally, more data points would be required to understand the detailed trends and dependence of p^* and V^* on $|\alpha|$ for different c_p.

was also shown to decrease the onset of secondary viscous fingering instabilities, such as tip-splitting or side-branching, in the displacements of suspensions in rectangular channels in [56, 60].

The dependence of the critical interfacial velocity, V^*, on the depth gradient, α, and the particle concentration, c_p, is shown in Fig. 3.5(b). For a fixed c_p, similar to the dependence on p^*, the general trend of V^* increases with an increasing gradient, $|\alpha|$. Also, for a fixed cell geometry, the critical velocity, V^*, decreases with an increasing c_p. The trend of V^* on c_p is particularly true for $c_p \geq 1$ $wt\%$ where the values of V^* increases gradually with an increasing c_p. However, for some α, we notice an interplay between the values of p^* for Newtonian solutions and suspensions of c_p = 1 $wt\%$. Besides, Figure 3.5(b) reveals a tendency to have a significant difference between the values of V^* for $c_p \leq 1$ $wt\%$ and $c_p \geq 2.5$ $wt\%$, which shows the destabilizing impact of the particles on the interface. We observe the values of V^* for $c_p \geq 2.5$ $wt\%$ are quite comparable and follow the same trend of a slight

increase from $\alpha = -1.6\times10^{-2}$ to $\alpha = -3.32\times10^{-2}$ before rising up more sharply. However, for $c_p = 1\ wt\%$, the increase of V^* with α is nearly linear. We notice p^* and V^* both increase with an increasing α and decrease with an increasing c_p. In fact, according to single-phase Darcy's law:

$$V = \frac{k}{\mu}\frac{\Delta p}{\Delta r} = \frac{k}{\mu}\frac{p - p_0}{r_0 - r} \tag{3.1}$$

with p_0 the pressure at the outlet of the cell. Therefore, for a constant viscosity, p^* and V^* are directly proportional to each other and so, it is not surprising to obtain similar results in their dependence on α and c_p. As μ_2 likely increases with an increasing c_p (see Tab. 3.1), we would expect from Fig. 3.5(a) to obtain an increasing V^* with an increasing c_p for each specific value of α. However, we notice that, for some α, the values of V^* for $c_p = 1\ wt\%$ are slightly bigger than the ones obtained for Newtonian solutions. The slight deviation between the results for p^* and V^* could be due to the time-changing viscosity, μ_2, as discussed in Appendix A.

3.4 Conclusions

In summary, we have experimentally demonstrated the suppression of viscous fingering instabilities when a gas displaces a suspension when the process takes place using a converging passage. For each gap gradient, α, and particle concentration, c_p, we can control the stability of the displacement by setting the injection pressure to a lower ($p < p^*$, stable) or higher ($p > p^*$, unstable) value than the critical pressure p^*. p^* was found to decrease with an increasing particle concentration but increase for a steeper gradient. Therefore, it implies that, for a fixed c_p, the stabilizing effect of the gradient on viscous fingering instabilities is more pronounced as α increases. On the other hand, the destabilizing effect by the particles becomes more critical as the concentration of particles in the displaced fluid increases. The critical interfacial velocity, V^*, has also been revealed to increase with an increasing $|\alpha|$ and decrease with an increasing c_p. Furthermore, the destabilizing effect of viscous fingering by the particles seems more important for $c_p \geq 2.5\ wt\%$ than for $c_p = 1\ wt\%$. A qualitative comparison between our current experimental results and previous ones in [106] or theo-

retical predictions by [80] revealed a good agreement in the dependence on α. However, a theoretical study of the displacement of a more viscous suspension by a less viscous fluid in a converging cell geometry is currently missing in the literature and would help us understand the mechanisms that control the interfacial stability and quantify the impact of the particles. Our experimental study reveals the possibility of tuning radial viscous fingering instabilities of complex suspensions by using inhomogeneous passages. The results of the dependence of p^* and V^* can be beneficial to design structures or predict the flow stability for processes where viscous fingering instabilities occur commonly.

Chapter 4

Conclusions and perspectives

In this work, the viscous fingering instability of radial immiscible displacements of Newtonian and suspension fluids in inhomogeneously confined passages has been experimentally investigated. For the first time, our experimental results show the control and, more specifically, inhibit viscous fingering of Newtonian and suspension fluids in radially tapered Hele-Shaw cells.

The experiments of viscous fingering of Newtonian fluids in tapered cell geometries revealed two distinct regimes of stable and unstable displacements. More specifically, the propagation of a stable front in a circular shape resulting in a full sweep of the displaced fluid was achieved at low injection flow rates, Q. On the other hand, at sufficient injection rate, classic Saffman-Taylor instabilities with the propagation of fingers have been commonly observed. By systematically repeating the process for different depth gradients, α, we were able to characterize the variation of the critical threshold depending on α. The critical flow rate, Q_c, has been found to increase with a steeper gap gradient, $|\alpha|$. By performing image analysis and tracking the position of the interface, we measured the critical interfacial velocity separating stable and unstable front propagation, and therefore the critical capillary number, Ca^*. For a fixed outer gap thickness, h_0, the critical Ca^* was revealed to increase with an increasing $|\alpha|$. In addition, the impact of h_0 on Ca^* was analyzed and showed no notable dependence of Ca^* for the range of h_0 explored. Our experimental results showed

good agreement with theoretical predictions by a linear stability analysis [80] and numerical simulations [89]. Therefore, for a fixed system of fluids, one can tune the design of a narrow passage and the injection process to control the fluid-fluid displacements.

Based on the experiments of radial viscous fingering with suspension fluids in inhomogeneous structures, surprisingly a full sweep of a suspension by gas injection is achieved despite the presence of micro-particles. The stability of the interface does not rely anymore only on the gap gradient α and the injection process, but also on the fluid properties with the particle concentration, c_p. We showed that, for a fixed α and c_p, the front propagation goes from stable to unstable when the injection pressure, p, overcomes a critical threshold. For a fixed c_p, the critical pressure, p^*, increases with a steeper gradient, $|\alpha|$. However, for a fixed α, p^* was found to decrease for a denser suspension. The stability diagram on p^* reveals the competition between the stabilizing effect of the converging gap gradient and the destabilizing one by the particles. The dependence of the critical velocity V^*, separating stable and unstable front propagation, on the gap gradient, α, and the particle concentration, c_p, was also analyzed. For a fixed c_p, V^* has been revealed to increase with an increasing $|\alpha|$ whereas, for a fixed α, V^* decreases with an increase in c_p. These experimental results of the viscous fingering problem with particles in tapered cells reveal the possible manipulation of the interfacial instabilities of suspension fluids using converging passages.

For the future investigation, it would be very interesting to develop a theoretical model explaining the behaviour of viscous fingering interfaces in tapered cells when pushing a suspension. The theoretical model would enable a quantitative comparison with the experimental results reported in Chapter 3 and a better understanding of the impact of particles on such moving interfaces.

Additionally, a possible extension of this work could be investigating the displacements of other complex fluids showing different rheological properties, such as a shear-dependent viscosity for instance, in converging cells. For the Saffman-Taylor problem, the displacement of a shear-thinning fluid by a Newtonian one could lead to interfaces more stable than those in the purely Newtonian case. However, the viscous fingering problem pushing a shear-

thickening fluid could result in a reduced stabilizing effect of the gradient. Furthermore, the destabilizing effect of the particles on the advancing interface is thought to be stabilizing when the particles are introduced in the displacing fluid instead [61]. Therefore, it could be of great interest for applications such as EOR to study the combination of both stabilizing effects of the gap gradient and particles on viscous fingering interfaces.

References

[1] Adrian Scheidegger et al. *The physics of flow through porous media*. University Of Toronto Press: London, 1958.

[2] Francis AL Dullien. *Porous media: fluid transport and pore structure*. Academic press, 1992.

[3] Morris Muskat, Ralph Dewey Wyckoff, et al. Flow of homogeneous fluids through porous media. 1937.

[4] R. A. Wooding and H. J. Morel-Seytoux. Multiphase Fluid Flow Through Porous Media. *Annu. Rev. Fluid Mech.*, 8(1):233–274, 1976.

[5] Francis Patton Bretherton. The motion of long bubbles in tubes. *Journal of Fluid Mechanics*, 10(2):166–188, 1961.

[6] Max Leva. Tower packings and packed tower design. 1953.

[7] Jacob Bear, Jean Marie Buchlin, et al. *Modelling and applications of transport phenomena in porous media*, volume 5. Springer, 1991.

[8] Peisheng Liu and Guo-Feng Chen. *Porous materials: processing and applications*. Elsevier, 2014.

[9] Lee A Segel. *Mathematical models in molecular cellular biology*. CUP Archive, 1980.

[10] Hans Meinhardt. *Models of biological pattern formation*. Academic Press, 1982.

[11] S. Hill. Channeling in packed columns. *Chem. Eng. Sci.*, 1(6):247–253, 1952.

[12] J. R. A. Pearson. The instability of uniform viscous flow under rollers and spreaders. *J. Fluid Mech.*, 7(4):481–500, 1960.

[13] E. Pitts and J. Greiller. The flow of thin liquid films between rollers. *J. Fluid Mech.*, 11(1):33–50, 1961.

[14] G. I. Taylor. Cavitation of a viscous fluid in narrow passages. *J. Fluid Mech.*, 16(4):595–619, 1963.

[15] M. J. Braun and R. C. Hendricks. An experimental investigation of the vaporous/gaseous cavity characteristics of an eccentric journal bearing. *ASLE transactions*, 27(1):1–14, 1984.

[16] K. J. Ruschak. Coating flows. *Annu. Rev. Fluid Mech.*, 17(1):65–89, 1985.

[17] M. Rabaud, S. Michalland, and Y. Couder. Dynamical regimes of directional viscous fingering: Spatiotemporal chaos and wave propagation. *Phys. Rev. Lett.*, 64(2):184, 1990.

[18] S Anderson, R Newell, A Soren, and N Richard. Prospects for Carbon Capture and Storage Technologies. *Annu. Rev. Environ. Resour.*, 29(1):109–142, 2004.

[19] Bert Metz, Ogunlade Davidson, Heleen de Coninck, Manuela Loos, and Leo Meyer. *Carbon dioxide capture and storage*. 2005.

[20] Y. Cinar, A. Riaz, and H. A. Tchelepi. In *SPE Annual Technical Conference and Exhibition*, number December. Society of Petroleum Engineers, 2007.

[21] Stefan Bachu. CO2 storage in geological media: Role, means, status and barriers to deployment. *Prog. Energy Combust. Sci.*, 34(2):254–273, 2008.

[22] H. E. Huppert and J. A. Neufeld. *Annu. Rev. Fluid Mech.*, 46(1):255–272, 2014.

[23] S. Buckley and M. Leverett. Mechanism of fluid displacement in sands. *Trans. AIME*, 146(1337):107–116, 1942.

[24] L. W. Lake. *Enhanced oil recovery*. Prentice Hall Englewood Cliffs, NJ, 1989.

[25] Martin Blunt, F John Fayers, and Franklin M Orr Jr. Carbon dioxide in enhanced oil recovery. *Energy Conversion and Management*, 34(9-11):1197–1204, 1993.

[26] Lars H Sjodahl. Ink flow on rotating rollers. *Am. Ink Maker*, 3:31, 1951.

[27] Pr Van Meurs et al. The use of transparent three-dimensional models for studying the mechanism of flow processes in oil reservoirs. 1957.

[28] GI Taylor. Deposition of a viscous fluid on the wall of a tube. *Journal of Fluid Mechanics*, 10(2):161–165, 1961.

[29] Henry Selby Hele-Shaw. The flow of water, 1898.

[30] L. Paterson. Radial fingering in a Hele Shaw cell. *J. Fluid Mech.*, 113(-1):513, 1981.

[31] P. G. Saffman and G. Taylor. The penetration of a fluid into a porous medium or hele-shaw cell containing a more viscous liquid. In *Proceedings of the Royal Society of London A: Mathematical, Physical and Engineering Sciences*, volume 245, pages 312–329. The Royal Society, 1958.

[32] R. L. Chouke, P. Van Meurs, and C. Van Der Poel. The instability of slow, immiscible, viscous liquid-liquid displacements in permeable media. *Pet. Trans. AIME*, 216:188–194, 1959.

[33] D. Bensimon, L. P. Kadanoff, S. Liang, B. I. Shraiman, and C. Tang. Viscous flows in two dimensions. *Rev. Mod. Phys.*, 58(4):977–999, 1986.

[34] G. M. Homsy. Viscous Fingering in Porous Media. *Annu. Rev. Fluid Mech.*, 19(1):271–311, 1987.

[35] P Tabeling, G Zocchi, and A Libchaber. An experimental study of the saffman–taylor instability. In *Dynamics of Curved Fronts*, pages 219–234. Elsevier, 1988.

[36] AJ DeGregoria and LW Schwartz. A boundary-integral method for two-phase displacement in hele-shaw cells. In *Dynamics of Curved Fronts*, pages 201–218. Elsevier, 1986.

[37] CW Park and GM Homsy. The instability of long fingers in hele–shaw flows. *The Physics of fluids*, 28(6):1583–1585, 1985.

[38] J Bataille. Stabilité d'un écoulement radial non miscible. In *Revue de l'Institut Français du Pétrole et Annales des Combustibles Liquides*, volume 23, page 1349, 1968.

[39] SD Howison. Fingering in hele-shaw cells. *Journal of Fluid Mechanics*, 167:439–453, 1986.

[40] J. D. Chen. Radial viscous fingering patterns in Hele-Shaw cells. *Exp. Fluids*, 5(6):363–371, 1987.

[41] Surendra P Gupta, James E Varnon, and Robert A Greenkorn. Viscous finger wavelength degeneration in hele-shaw models. *Water Resources Research*, 9(4):1039–1046, 1973.

[42] Jing-Den Chen. Growth of radial viscous fingers in a hele-shaw cell. *Journal of Fluid Mechanics*, 201:223–242, 1989.

[43] SN Rauseo, PD Barnes Jr, and JV Maher. Development of radial fingering patterns. *Physical Review A*, 35(3):1245, 1987.

[44] I. Bischofberger, R. Ramachandran, and S. R. Nagel. An island of stability in a sea of fingers: emergent global features of the viscous-flow instability. *Soft matter*, 11(37):7428–7432, 2015.

[45] Hendrik Van Olphen. *An introduction to clay colloid chemistry: for clay technologists, geologists, and soil scientists*. 1977.

[46] Ronald G Larson. The structure and rheology of complex fluids (topics in chemical engineering). *Oxford University Press, New York - Oxford*, 86:108, 1999.

[47] D Bonn, H Kellay, M Bräunlich, M Ben Amar, and J Meunier. Viscous fingering in complex fluids. *Physica A: Statistical Mechanics and its Applications*, 220(1-2):60–73, 1995.

[48] Anke Lindner, Daniel Bonn, and Jacques Meunier. Viscous fingering in complex fluids. *Journal of Physics: Condensed Matter*, 12(8A):A477, 2000.

[49] CK Chan and NY Liang. Observations of surfactant driven instability in a hele-shaw cell. *Physical review letters*, 79(22):4381, 1997.

[50] Anke Lindner, Daniel Bonn, and Jacques Meunier. Viscous fingering in a shear-thinning fluid. *Physics of Fluids*, 12(2):256–261, 2000.

[51] Anke Lindner, Philippe Coussot, and Daniel Bonn. Viscous fingering in a yield stress fluid. *Physical Review Letters*, 85(2):314, 2000.

[52] Nahid Maleki-Jirsaraei, Anke Lindner, Shahin Rouhani, and Daniel Bonn. Saffman–taylor instability in yield stress fluids. *Journal of Physics: Condensed Matter*, 17(14):S1219, 2005.

[53] A Eslami and SM Taghavi. Viscous fingering regimes in elasto-visco-plastic fluids. *Journal of Non-Newtonian Fluid Mechanics*, 243:79–94, 2017.

[54] H Zhao and JV Maher. Associating-polymer effects in a hele-shaw experiment. *Physical Review E*, 47(6):4278, 1993.

[55] Jordi Ignes-Mullol, H Zhao, and JV Maher. Velocity fluctuations of fracturelike disruptions of associating polymer solutions. *Physical Review E*, 51(2):1338, 1995.

[56] Masami Kawaguchi. Viscous fingering of silica suspensions dispersed in polymer fluids. ACS Publications, 2004.

[57] E Lemaire, P Levitz, G Daccord, and H Van Damme. From viscous fingering to viscoelastic fracturing in colloidal fluids. *Physical review letters*, 67(15):2009, 1991.

[58] Masami Kawaguchi, Sayaka Yamazaki, Kenji Yonekura, and Tadaya Kato. Viscous fingering instabilities in an oil in water emulsion. *Physics of Fluids*, 16(6):1908–1914, 2004.

[59] Masami Kawaguchi, Kyoko Makino, and Tadaya Kato. Viscous fingering patterns of silica suspensions in polymer solutions: effects of viscoelasticity and gravity. *Physica A: Statistical Mechanics and its Applications*, 246(3-4):385–398, 1997.

[60] Naoki Kagei, Daisuke Kanie, and Masami Kawaguchi. Viscous fingering in shear thickening silica suspensions. *Physics of Fluids*, 17(5):054103, 2005.

[61] H Tang, W Grivas, D Homentcovschi, J Geer, and T Singler. Stability considerations associated with the meniscoid particle band at advancing interfaces in hele-shaw suspension flows. *Physical Review Letters*, 85(10):2112, 2000.

[62] Ilyesse Bihi, Michael Baudoin, Jason E Butler, Christine Faille, and Farzam Zoueshtiagh. Inverse saffman-taylor experiments with particles lead to capillarity driven fingering instabilities. *Physical review letters*, 117(3):034501, 2016.

[63] Feng Xu, Jungchul Kim, and Sungyon Lee. Particle-induced viscous fingering. *Journal of Non-Newtonian Fluid Mechanics*, 238:92–99, 2016.

[64] J. Kim, F. Xu, and S. Lee. Formation and destabilization of the particle band on the fluid-fluid interface. *Phys. Rev. Lett.*, 118(7):074501, 2017.

[65] I. Bischofberger, R. Ramachandran, and S. R. Nagel. Fingering versus stability in the limit of zero interfacial tension. *Nat. Comm.*, 5(1):5265, 2014.

[66] Francisco M Rocha and José A Miranda. Manipulation of the saffman-taylor instability: A curvature-dependent surface tension approach. *Physical Review E*, 87(1):013017, 2013.

[67] M. Trojer, M. L. Szulczewski, and R. Juanes. Stabilizing Fluid-Fluid Displacements in Porous Media Through Wettability Alteration. *Phys. Rev. Appl.*, 3(5):1–8, 2015.

[68] B. Zhao, C. W. MacMinn, and R. Juanes. Wettability control on multiphase flow in patterned microfluidics. *Proc. Natl. Acad. Sci. U.S.A.*, 113(37):10251–6, 2016.

[69] EA Brener, DA Kessler, H Levine, and W-J Rappei. Selection of the viscous finger in the 90 geometry. *EPL (Europhysics Letters)*, 13(2):161, 1990.

[70] S. Li, J. S. Lowengrub, J. Fontana, and P. Palffy-Muhoray. Control of viscous fingering patterns in a radial Hele-Shaw cell. *Phys. Rev. Lett.*, 102(17):1–4, 2009.

[71] Alexander Leshchiner, Matthew Thrasher, Mark B Mineev-Weinstein, and Harry L Swinney. Harmonic moment dynamics in laplacian growth. *Physical Review E*, 81(1):016206, 2010.

[72] Ching-Yao Chen, C-W Huang, L-C Wang, and José A Miranda. Controlling radial fingering patterns in miscible confined flows. *Physical Review E*, 82(5):056308, 2010.

[73] Eduardo O Dias and José A Miranda. Control of radial fingering patterns: A weakly nonlinear approach. *Physical Review E*, 81(1):016312, 2010.

[74] Z. Zheng, H. Kim, and H. A. Stone. Controlling viscous fingering using time-dependent strategies. *Phys. Rev. Lett.*, 115(17):1–5, 2015.

[75] D. Pihler-Puzović, R. Périllat, M. Russell, A. Juel, and M. Heil. Modelling the suppression of viscous fingering in elastic-walled Hele-Shaw cells. *J. Fluid Mech.*, 731(Hull 1999):162–183, 2013.

[76] E. O. Dias, E. Alvarez-Lacalle, and J. A. Carvalho, M. S. Miranda. Minimization of viscous fluid fingering: A variational scheme for optimal flow rates. *Phys. Rev. Lett.*, 109(14):1–5, 2012.

[77] E. O. Dias, F. Parisio, and J. A. Miranda. Suppression of viscous fluid fingering: A piecewise-constant injection process. *Phys. Rev. E*, 82(6):1–4, 2010.

[78] D. Pihler-Puzović, P. Illien, M. Heil, and A. Juel. Suppression of complex fingerlike patterns at the interface between air and a viscous fluid by elastic membranes. *Phys. Rev. Lett.*, 108(7):1–5, 2012.

[79] J. R Lister, G. G Peng, and J. A Neufeld. Viscous control of peeling an elastic sheet by bending and pulling. *Phys. Rev. Lett.*, 111(15):154501, 2013.

[80] T. T. Al-Housseiny, I. C. Christov, and H. A. Stone. Two-phase fluid displacement and interfacial instabilities under elastic membranes. *Phys. Rev. Lett.*, 111(3):1–5, 2013.

[81] Draga Pihler-Puzović, Anne Juel, Gunnar G Peng, John R Lister, and Matthias Heil. Displacement flows under elastic membranes. part 1. experiments and direct numerical simulations. *Journal of Fluid Mechanics*, 784:487–511, 2015.

[82] D Halpern and OE Jensen. A semi-infinite bubble advancing into a planar tapered channel. *Physics of Fluids*, 14(2):431–442, 2002.

[83] T Maxworthy. The effect of a stabilising gradient on interface morphology. In *Interfaces For The 21st Century: New Research Directions In Fluid Mechanics And Materials Science*, pages 3–20. World Scientific, 2002.

[84] H Zhao, J Casademunt, C Yeung, and JV Maher. Perturbing hele-shaw flow with a small gap gradient. *Physical Review A*, 45(4):2455, 1992.

[85] E. O. Dias and J. A. Miranda. Finger tip behavior in small gap gradient Hele-Shaw flows. *Phys. Rev. E*, 82(5):1–7, 2010.

[86] T. T. Al-Housseiny, P. A. Tsai, and H. A. Stone. Control of interfacial instabilities using flow geometry. *Nat. Phys.*, 8(10):747–750, 2012.

[87] T. T. Al-Housseiny and H. A. Stone. Controlling viscous fingering in tapered Hele-Shaw cells. *Phys. Fluids*, 25(9):092102, 2013.

[88] Eduardo O Dias and José A Miranda. Taper-induced control of viscous fingering in variable-gap hele-shaw flows. *Physical Review E*, 87(5):053015, 2013.

[89] S. J. Jackson, H. Power, D. Giddings, and D. Stevens. The stability of immiscible viscous fingering in hele-shaw cells with spatially varying permeability. *Comput. Methods Appl. Mech. Eng.*, 320:606–632, 2017.

[90] J. C. Grenfell-Shaw and A. W. Woods. The instability of a moving interface in a narrow tapering channel of finite length. *J. Fluid Mech.*, 831:252–270, 2017.

[91] Siti Aminah Setu, Ioannis Zacharoudiou, Gareth J Davies, Denis Bartolo, Sébastien Moulinet, Ard A Louis, Julia M Yeomans, and Dirk GAL Aarts. Viscous fingering at ultralow interfacial tension. *Soft Matter*, 9(44):10599–10605, 2013.

[92] Lautaro Díaz-Piola, Ramon Planet, Otger Campàs, Jaume Casademunt, and Jordi Ortín. Fluid front morphologies in gap-modulated hele-shaw cells. *Physical Review Fluids*, 2(9):094006, 2017.

[93] A. L. Hazel, M. Pailha, S. J. Cox, and A. Juel. Multiple states of finger propagation in partially occluded tubes. *Phys. Fluids*, 25(6):021702, 2013.

[94] P. H. Anjos, E. O. Dias, and J. A. Miranda. Radial fingering under arbitrary viscosity and density ratios. *Phys. Rev. Fluids*, 2(8):084004, 2017.

[95] SS Park and Douglas J Durian. Viscous and elastic fingering instabilities in foam. *Physical review letters*, 72(21):3347, 1994.

[96] Saraswathi Enjamoori, Jalel Azaiez, and Brij B Maini. Experimental investigation of viscous fingering instabilities in emulsions displacements. *International Journal of Emerging Multidisciplinary Fluid Sciences*, 2(4), 2010.

[97] A. Buka, P. Palffy-Muhoray, and Z. Rácz. Viscous fingering in liquid crystals. *Phys. Rev. A*, 36:3984–3989, Oct 1987.

[98] C Chevalier, A Lindner, M Leroux, and E Clément. Morphodynamics during air injection into a confined granular suspension. *Journal of Non-newtonian fluid mechanics*, 158(1-3):63–72, 2009.

[99] Jon Alm Eriksen, Renaud Toussaint, Knut Jørgen Måløy, Eirik Flekkøy, Olivier Galland, and Bjørnar Sandnes. Pattern formation of frictional fingers in a gravitational potential. *Phys. Rev. Fluids*, 3:013801, Jan 2018.

[100] Pawel Pieranski. Two-dimensional interfacial colloidal crystals. *Physical Review Letters*, 45(7):569, 1980.

[101] P Singh and DD Joseph. Fluid dynamics of floating particles. *Journal of Fluid Mechanics*, 530:31–80, 2005.

[102] Dominic Vella, Paul D Metcalfe, and Robert J Whittaker. Equilibrium conditions for the floating of multiple interfacial objects. *Journal of Fluid Mechanics*, 549:215–224, 2006.

[103] Spencer Umfreville Pickering. Cxcvi.—emulsions. *J. Chem. Soc., Trans.*, 91:2001–2021, 1907.

[104] Roy J Furbank and Jeffrey F Morris. Pendant drop thread dynamics of particle-laden liquids. *International journal of multiphase flow*, 33(4):448–468, 2007.

[105] Merlijn S van Deen, Thibault Bertrand, Nhung Vu, David Quéré, Eric Clément, and Anke Lindner. Particles accelerate the detachment of viscous liquids. *Rheologica Acta*, 52(5):403–412, 2013.

[106] Grégoire Bongrand and Peichun Amy Tsai. Manipulation of viscous fingering in a radially tapered cell geometry. *Physical Review E*, 97(6):061101, 2018.

[107] SG Mallinson, GD McBain, and GD Horrocks. Viscosity and surface tension of aqueous mixtures. 2016.

[108] A Karnis and SG Mason. The flow of suspensions through tubes vi. meniscus effects. *Journal of Colloid and Interface Science*, 23(1):120–133, 1967.

[109] Nian-Sheng Cheng. Formula for the viscosity of a glycerol- water mixture. *Industrial & engineering chemistry research*, 47(9):3285–3288, 2008.

[110] K Drucker and E Moles. Gas solubility in aqueous solutions of glycerol and isobutyric acid. *Z. Phys. Chem. Stoechiom. Verwandtschaftsl*, 75:405–436, 1910.

[111] A von Hammel. Gaslöslichkeit in wässerigen lösungen von glycerin und chloralhydrat. *Zeitschrift für Physikalische Chemie*, 90(1):121–125, 1915.

[112] Rubin Battino. Nitrogen and air. 1982.

[113] CE Beecher, IP Parkhurst, et al. Effect of dissolved gas upon the viscosity and surface tension of crude oil. *Transactions of the AIME*, (01):51–69, 1926.

Appendix A

Time-varying viscosity of the water-glycerol solutions used

Here, we report the measurements and observations made about the changes of the viscosity μ_2 of the water-glycerol solutions (used in the experiments of suspension fluid, described in Ch.3) in time. After performing a set of experiments, we noticed a qualitative change in the viscosity of a water-glycerol suspension of c_p = 1 $wt\%$. Therefore, we decided to perform rheological measurements of the solution which was used in the experiments using a concentric cylinder. The rheological data obtained confirmed the time variation of the viscosity: μ_2 decreased from 157 cP before the experiments to μ_2 = 69 cP afterwards (see ▲ in Fig. A.1). We repeated the measurements for the suspension solution of c_p = 2.5 $wt\%$ (■) and observed the same trend: right after mixing particles with the solution, μ_2 = 160 cP whereas μ_2 = 50 cP after being used for the experiments (corresponding to the elapsed time of 10 days). Hence, this likely implies μ_2 may not be constant throughout all the set of experiments. An empirical model of the viscosity of water-glycerol solutions based on their composition was derived in [109]. For a mixture of water-glycerol with 12.5 $wt\%$ of water, the viscosity of the mixture is 144 cP [109], which is close to the value of 146 cP found for c_p = 0 $wt\%$ (see ● in Fig. A.1). In comparison, our experimental values obtained before the experiments (i.e., t = 0 days) are in good agreement.

Therefore, after completing the viscous fingering experiments, we conducted systematically rheological measurements of a unused sample of c_p = 2.5 $wt\%$ to assess how the viscosity evolves with time. A sample was extracted from the main solution before performing the experiments and kept in a closed beaker. Figure A.1 shows the time-varying viscosity μ_2 of the unused sample, for c_p = 2.5 $wt\%$ (□). The data show a dramatic reduction in the suspension viscosity of the water-glycerol suspension, decreasing from 160 cP to 60 cP. After 10 days, we can see that the viscosity obtained from the unused sample, μ_2 = 134 cP, is significantly bigger than μ_2 obtained for the solution used in the experiments. The solution viscosity seems to decay faster once being used in the experiments, but a significant decrease is still observed for a solution at rest, and later during the rheological measurements (after t = 10 days, see Fig. A.1).

An explanation for the decrease in viscosity could be the dissolution of gas into the solu-

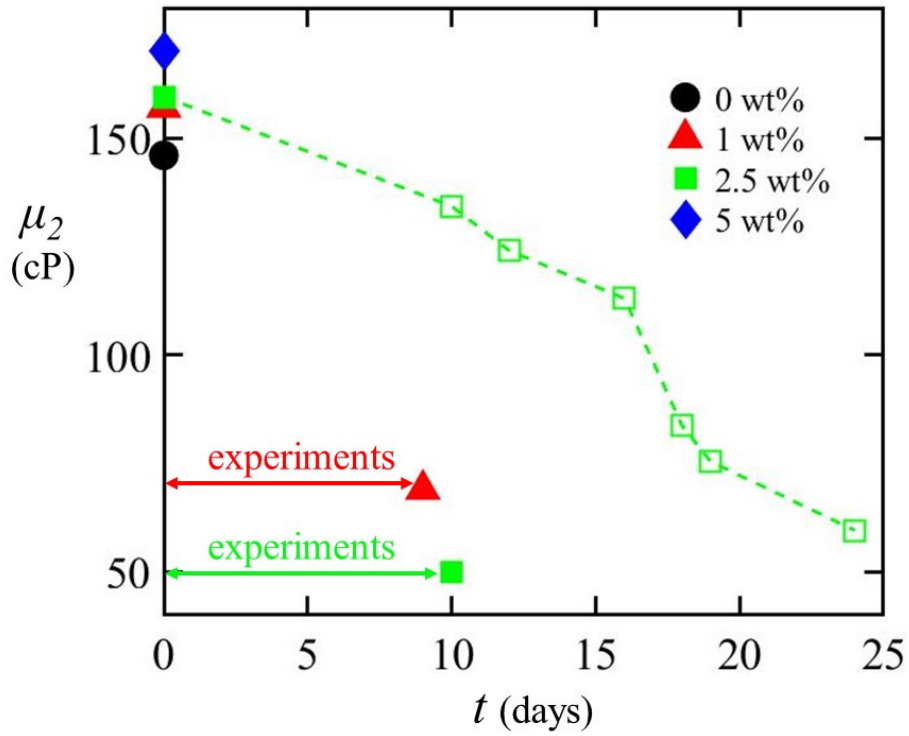

Figure A.1: Time-evolution of the viscosity of the water-glycerol suspensions used in the experiments (●, ▲, ■, ♦), and the unused sample of c_p = 2.5 $wt\%$ (□). Measurements were performed via a rheometer, and 2-5 times for each point.

tions and, in the literature, we found evidence that air and nitrogen dissolve in water-glycerol mixtures [110, 111, 112]. Globally, the solubility of air and nitrogen in glycerol is smaller than in pure water and decreases with an increasing glycerol weight concentration[112]. The Ostwald coefficients—the ratio of the volume of gas absorbed to the volume of the absorbing liquid—for a mixture with a similar water concentration as the experimental solutions, at standard conditions of temperature and pressure, are about 10^{-3}–10^{-2} [110, 111]. Since gas is much less viscous compared to the aqueous mixtures of glycerol, even if a tiny quantity would dissolve, likely the viscosity of the overall mixture would decrease significantly. Indeed, the impact of gas dissolution on the viscosity of crude oil was investigated in [113] and revealed percentages of reduction in the viscosity up to 70 % when the gas saturates the solution. Furthermore, the reason why after ten days the viscosity of the unused sample decayed to "only" 134 cP whereas the one of the experimental solution decreased to 50 cP could find an explanation. Indeed, the experimental solution was present in a shallow container (with a large surface area), directly exposed to the ambient air, and regularly mixed whereas the unused sample was remain untouched in a closed beaker.

The nonlinearity of the time-variation of the sample viscosity for $c_p = 2.5\ wt\%$, combined to the fact the time taken to perform experiments varied from a concentration to another, makes it too complex to know the exact viscosity value for each specific configuration of α and c_p. Moreover, we have not found any literature dealing with the impact of gas dissolution on the viscosity of water-glycerol mixtures. As a consequence, without detailed data of $\mu_2(t)$, we could not accurately characterize the stability of the interface in terms of the capillary number Ca since the value of the viscosity at $t = 0$ is not physically relevant for the problem. Therefore, we analyzed the flow instabilities using critical gauge pressure imposed, p^*, and critical flow velocity, V^*, at the interface.